Enhancement of Lift and Drag Characteristics of an Oscillating Airfoil in Deep Dynamic Stall Using Plasma Actuation

Siddhartha Mukherjee[1] and Subrata Roy[2]
Computational Plasma Dynamics Laboratory and Test Facility
Mechanical and Aerospace Engineering Department
University of Florida, Gainesville, FL 32611-6300

The two dimensional flow past an oscillating NACA 0012 airfoil at Re = 1.35 x 10^5 is simulated using a large eddy simulation model and subsequently, the influence of plasma actuation on flow control over such an oscillating airfoil is theoretically predicted. Simulation results without plasma actuation were benchmarked with earlier reported experimental data. The formation, growth and separation of the vortical structures along the airfoil have been studied without and with the influence of plasma body force generated by the dielectric barrier discharge actuators. We present results for plasma actuators placed at the leading edge, mid chord and trailing edge locations in both co-flow and counter flow configurations. The force due to the actuator for a length of 1.5-2.0 cm varied in the range of 4-15 kN/m^3 and this was predicted from a force approximation model. Our results show that depending upon the location of the actuator up to 29.2% more lift and 12.5% less drag can be obtained. Such predicted improvement in the lift and drag characteristics through the use of plasma actuation indicate a very useful application of such flow control device in enhancing the performance of oscillating airfoils.

Nomenclature

α	=	Angle of attack
β_x, β_y	=	Functions of dielectric material
c	=	Chord Length
C_L	=	Coefficient of Lift
C_D	=	Coefficient of Drag
C_M	=	Coefficient of Moment
ρ	=	Density of air
f	=	Oscillation frequency
$\vec{F}$	=	Force due to a plasma actuator
F_{x0}, F_{y0}	=	Electrodynamic force constants
k	=	Reduced frequency
φ_0	=	Amplitude of applied rf potential
p	=	Pressure of fluid
Re	=	Reynolds Number
St	=	Strouhal Number
σ	=	Standard Deviation
$\vec{\bar{t}}$	=	Stress tensor
t	=	Instantaneous Time
T_c	=	Characteristic Time
U_∞	=	Free stream velocity
$\vec{v}$	=	velocity of fluid
ω	=	Angular velocity of oscillation
x_0	=	Midpoint of the distance between the rf electrode and the grounded electrode
x	=	Global abscissa
x_c	=	Abscissa of origin in local airfoil co-ordinate
x'	=	Abscissa in local airfoil co-ordinate
y	=	Global ordinate

[1] Graduate Research Assistant, AIAA Student Member, Emal: Siddhartha@ufl.edu
[2] Associate Professor, AIAA Associate Fellow, E-mail: roy@ufl.edu

y_0	=	Dielectric surface
y_c	=	Ordinate of origin in local airfoil co-ordinate
y'	=	Ordinate in local airfoil co-ordinate

Subscripts

P	=	Total number of oscillation cycles in a simulation
T	=	Total number of time steps in a cycle

I. Introduction

Airfoils that stall at modest angles of attack have limited maneuverability and agility. The problem of unsteady airfoil motion and dynamic retreating blade problem limiting the high speed performance of rotorcrafts is well known and documented[9]. This problem serves as a great motivation in increasing lift generated by an oscillating airfoil and delaying dynamic stall. Today, with the additional need for novel designs involving flapping airfoils with applications in mini and Micro Air Vehicles, various techniques are being explored that can enhance the stall angle of attack and increase the aerodynamic characteristics of oscillating airfoils.

It is now well established[5,6,7,8,9] that flow over oscillating airfoils separate even at slightly higher angles of attack and the flow is characterized by the formation of several eddies and vortices. Lee and Gerontakos[1] found that while flow separation at lower angles of attack is detrimental to lift, the Leading Edge Vortex (LEV) that is formed at larger angles of attack and while it is attached to the airfoil surface causes significantly larger values of the lift compared to that of a static airfoil. Further increase in the angle of attack causes the LEV to grow and envelop almost the entire surface of the airfoil until it sheds off the trailing edge, leading to a sudden and drastic decrease in lift. Delaying of the shedding of the LEV can be highly beneficial, and hence control of flow separation at lower angles of attack can increase lift enhancing the performance of an oscillating airfoil. This paper attempts to evaluate the potential of plasma actuators in achieving these aforementioned benefits on a flapping airfoil through numerical simulations.

While flapping airfoils and wings have applications both for rotorcrafts and MAVs, flapping winged flight poses a serious challenge. Natural fliers have very complicated wing kinematics which helps to create vortices and other unsteady fluid dynamic phenomenon, as discussed before that is responsible for lift generation and maneuvers. The flight kinematics is also aided by their flexible wings which deform dynamically during flight. Insect wings have structural nonlinearity with exponential variation of chord wise and span wise flexural stiffness as shown by Combes and Daniel[1, 2] and subsequently, researchers like Mountcastle and Daniel[3] have showed that dynamic wing bending is beneficial for both aerodynamic force production and maneuvers in insect flight.

The field of flapping wing aerodynamics has been inspired by flying animals such as birds, bats, insects and efficient swimmers like fish, which have extraordinary flying and swimming capabilities. As put forth by Ashraf et al.[4], there has been a surge of interest of researchers in this field in recent times due to the possibilities of flapping wing powered micro aerial vehicles (MAVs) and submerged vehicles. Research on natural fliers with potential application in MAVs by Sane[5], Ellington[6, 7] and Zbikowski[8] have predicted the existence of various unsteady aerodynamic phenomena. At low Reynolds numbers, these include flow separation and wake formation, LEVs and dynamic stall. Furthermore, Ellington[6] showed that LEVs increase lift significantly in natural fliers and is one of the main unsteady phenomena sustaining flapping winged flight. This has also been found to be true for oscillating airfoils. Experimental investigation of flow past a NACA 0012 airfoil by Lee and Gerontakos[9] has revealed that the airfoil stalled at an angle of attack of 13° when static. When the same airfoil was oscillated in a wind tunnel at angles of attack higher than the static stall angle, an LEV was found to form at an angle of about 21.9°. This LEV increased in strength as the angle of attack increased up to 24.4° and at this angle, the measured maximum coefficient of lift C_{Lmax} was reported to be 2.44, as compared to 0.92 for a static airfoil.

Various techniques are being explored today to improve the aerodynamic characteristics of bio-inspired MAVs. While modeling and implementation of insect like flexible wings is a challenge in itself, attempts are being made to incorporate this feature in MAVs. Bio-mimicked flexible wings using membranes and vein like framework have been used by Ifju. et al.[10, 11] to increase the aerodynamic performance and stall angle of attack in MAVs. Alternatively, non-uniform cantilever beam type modeling of the wing for MAV applications has also been suggested, like the model of Ganguli et al.[12] While wing flexibility is advantageous, controlling the fluid structure interaction can be even beneficial. Several researchers like Jacob[13], Cox[14] and Lian et al.[15] have been exploring the possible use of smart or adaptive structures and aero elastic control of wings with structural nonlinearity using piezoelectric actuation.

The above discussion underlines the need for flow modifying mechanisms that can create the necessary fluid dynamic effects for realizing flapping winged flight. Besides fluid structure interactions, alternative techniques for flow modification are also being explored. Plasma-based flow control techniques exploiting electromagnetic forces are currently of considerable interest. Particularly attractive properties stem from the absence of moving parts and lack of mechanical inertia, which permits instantaneous deployment over a broad range of frequencies.

Dielectric Barrier Discharge plasma (DBD) plasma actuators typically consist of two copper electrodes separated by a dielectric medium. It can be laminated to the surface of the airfoil at receptive locations. Roth et.al[16] and later Corke et. al[17] described that when sufficiently high ac voltage is applied between the two electrodes (3-12 kV) there occurs local ionization of the surrounding air above a threshold electric field of around 30 kV/cm generating an electrodynamic body force. The ionization of the air is a dynamic process and this body force is the mechanism for active aerodynamic control. The momentum imparted by the actuator can be controlled by the geometric properties of the actuator, as well as the applied potential difference across the dielectric medium. The range of this body force can range from kN/m^3 to MN/m^3.

The body force per unit volume of plasma is derived from first principles and utilizes models for the time and space dependence of the air ionization on the input voltage amplitude, frequency, electrode geometry and dielectric properties. Such models have been developed by Singh and Roy[18, 19]. The actuators can be placed in co-flow or counter flow configurations. In the co-flow arrangement, the horizontal component of the plasma body force is in the direction along the incoming flow (see Fig. 1a) and offers momentum enhancement via favorable pressure gradient in the near wall region helping the flow to remain attached or separation to be delayed. In the counter flow arrangement (in Fig. 1b), the horizontal component of the body force is in the direction opposite to that of the freestream, which can trigger earlier separation and transition by introducing adverse pressure gradients.

To investigate the scope of DBD actuators in Low Reynolds number flow control Shyy et al.[20] simulated flow past an SD7003 airfoil at various angles of attack and found that there was a consistent increase in lift and decrease in drag, especially at high angles of attack. To tackle the problem of retreating blade stall (RBS) in helicopters, Corke *et al.*[21, 22] experimentally studied the effects of plasma actuation at the leading edge of an oscillating airfoil and found that it provided a significant increase in lift when integrated over the entire cycle compared to the no-actuation case. The observable increase in lift was more pronounced at lower angles of attack during the pitch down portion of the oscillation cycle. These results provide greater motivation for our studies in exploring plasma actuation technology in flapping wings for MAVs and rotorcrafts.

The aim of our present work is to computationally explore the potential of plasma actuation based flow control of airfoil which is oscillated sinusoidally at a Reynolds number of 1.35×10^5. The airfoil chosen in this case is a symmetrical NACA 0012 airfoil which has a maximum thickness of 12% at 30% of its chord. We use plasma force derived using first principles into large eddy simulation (LES) model in FLUENT 12.0 commercial solver for our flow simulations. Compared to URANS and other turbulence models in FLUENT, LES is better adept at capturing the flow physics comprising of numerous eddies and other turbulent flow phenomenon typical of this type of flow. Due to computational limitations, we have restricted our studies to a two dimensional model while a full three-dimensional model is being considered for the future. We have also based and benchmarked our case of flow past the oscillating airfoil without any plasma actuation with the experimental data of Lee and Gerontakos[9], which presented a 2D description of the identical case. Similar 2D studies on this case have been carried out in FLUENT by Wang *et al.*[23] using URANS and DES models.

To study and develop a strategy for plasma actuation of the oscillating NACA 0012 airfoil, we have carried out simulations with both co-flow and counter flow arrangement of the plasma actuator placed at the leading edge, mid chord and trailing edge locations on the upper surface of the airfoil

II. Model Description

A. Case Studied

The NACA 0012 airfoil used in this study has a chord length of $c=0.15m$, that undergoes sinusoidal plunging motion with an angle of attack of the type $\alpha(t) = \alpha_{mean} + \Delta\alpha \sin(\omega t)$ around an axis located at quarter of its chord length ($0.25c$) from the leading edge. In order to validate our data with experiment, we have chosen a sinusoidal motion same as that of the available experimental data, given by $\alpha=10°+15°\sin(\omega t)$. The airfoil oscillates in air with a reduced frequency ($k=\omega c/2U_\infty$) of 0.1, which corresponds to an angular velocity (ω) of 18.67 rad/s and a physical oscillating frequency of 2.97 Hz. For a freestream velocity (U_∞) of 14 m/s, the chord Reynolds number is 1.35×10^5. The Strouhal number based on chord length ($St=fc/U_\infty$) for this case is 0.03. The choice of these parameters gives us a scope to validate our model with experiment allowing us to use it in future for flow control simulations.

It is worthwhile mentioning that Ellington[5] had found that reduced frequencies in natural fliers vary from 0.1 to 0.3, small to big insects or birds. Large insects have Reynolds number between 5×10^3 and 10^4 while, the smallest of insects can have Reynolds numbers as low as 10.

B. Mesh

The grid used for simulations is shown in Fig. 2, has been designed using GAMBIT. It is an unstructured C-Type mesh with a total of 124744 triangular elements and 62372 nodes. This was achieved by adjusting the first cell size equal to $10^{-5}c$. For a desired y+ value of 0.7 or O(1), the estimated wall distance was 1.5×10^{-5} m, which explains our design of the grid. To ensure free stream condition at the boundaries, the inlet is situated at 12.5 chord lengths upstream from the airfoil while the outlet is 21 chord lengths downstream from the airfoil

C. Solver details and Equation system

The characteristic time ($T_c=2\pi/\omega$) for this simulation was taken to be the time period for one complete oscillation. Numerical time step was taken to be $0.001T_c$ and thus one oscillation comprised 1000 time steps. The sinusoidal pitching motion of the airfoil is achieved by the dynamic meshing feature of ANSYS FLUENT 12.0 commercial solver. The oscillatory motion of the airfoil is specified using a user defined function (UDF) subroutine attached to the solver. The dynamic meshing feature used here employs all of spring based smoothing, layering and remeshing techniques. Globally, the grid remains stationary while the airfoil oscillates like a rigid body while mesh is adapted locally and dynamically. For incompressible flow approximation we use a standard pressure based algorithm and a 2d Smagorinsky-Lilly LES model with a Smagorinsky constant (C_s) of 0.1. Pressure-velocity coupling is done by the semi-implicit method for pressure linked equations (SIMPLE). First order implicit solver for time is used for the two dimensional LES model. For spatial discretization, momentum is calculated by bounded central differencing, while gradient is calculated using the Green-Gauss cell based method.

Fluent solves the conservation equations for mass and momentum given by Eq. 1 and Eq. 2. The plasma actuator body force is incorporated into the momentum equation as $\vec{F}$.

$$\nabla.(\vec{v}) = 0 \tag{1}$$

$$\frac{\partial}{\partial t}(\vec{v}) + (\vec{v}.\nabla)\vec{v} = -\frac{\nabla p}{\rho} + \frac{\nabla.(\vec{\tau})}{\rho} \tag{2}$$

Here ρ is the density of air, $\vec{v}$ is the velocity, p is the pressure and $\vec{\tau}$ is the stress tensor. We have ignored the effect of gravity in our simulations and hence it has been omitted from the momentum equation. The body force term due to plasma actuation $\vec{F}$ has been approximately calculated using the first principles based reduced order model of Singh and Roy[24]. The model constitutes a functional relationship between the electrodynamic force and electrical and physical control parameters, approximated and numerically tested for air which was obtained by employing a load based first principles approach and solving the governing equations of charged and neutral species using the Poisson's equation. This model gives an approximate electrodynamic force for direct implementation into Navier Stokes equations. The original force equation is given by Eq. 3.

$$\vec{F} = F_{x0}j_0^4 \exp[-\{\frac{(x-x_0-\overline{y-y_0})}{y}\}^2 - b_x(y-y_0)^2]\hat{i} \pm F_{y0}j_0^4 \exp\{-(\frac{x-x_0}{y})^2 - b_y(y-y_0)^2\}\hat{j} \tag{3}$$

Here F_{x0} and F_{y0} are electrodynamic force constants which have been obtained by solving the air plasma equations. β_x and β_y are functions of the dielectric material while x_0 is the midpoint of the distance between the rf electrode and the grounded electrode. The height of the dielectric surface is given by y_0. This equation is modified transformed into the local co-ordinate system following the curvature of the airfoil its dynamic position at any instant of time. Eq.4 gives the equation of the surface of the NACA 0012 airfoil, which is obtained from the generalized equation for a NACA airfoil and a chord length of 15cm.

$$y = \frac{0.12}{0.2} \times 0.15 \times \left[0.2969\sqrt{\frac{x}{0.15}} - 0.1260\left(\frac{x}{0.15}\right) - 0.3315\left(\frac{x}{0.15}\right)^2 + 0.2843\left(\frac{x}{0.15}\right)^3 - 0.1015\left(\frac{x}{0.15}\right)^4 \right] \tag{4}$$

When the airfoil has no angle of attack the global origin coincides with the origin of the airfoil. As the airfoil rotates about an axis located at the quarter chord location, the global co-ordinates are shifted to the local coordinates using Eqs. 5-8.

$$x_c = \frac{c}{4}(1 - \cos\alpha) \tag{5}$$

$$y_c = \frac{c}{4}\sin\alpha \tag{6}$$

$$x' = (x - x_c)\cos\alpha - (y - y_c)\sin\alpha \tag{7}$$

$$y' = (x - x_c)\sin\alpha + (y - y_c)\cos\alpha \tag{8}$$

Here x and y are the global Cartesian co-ordinates, whereas x' and y' are local Cartesian co-ordinates. The local origin is given by x_c and y_c. The surface of the airfoil at any angle of attack is obtained by using Eq.7 in Eq. 4. The direction tangential to the airfoil surface is obtained by using Eq. 7 in the derivative of Eq. 4. The plasma force at any angle of attack is then applied at every point of its domain by resolving it into stream wise and normal components.

For the plasma actuator, the region of influence was chosen to be 1.5 to 2 cm wide in the chordwise direction and extending 2cm normal to the surface of the airfoil. This plasma force was incorporated into the FLUENT solver as momentum source terms in the x and y direction using another User Defined Function (UDF) subroutine. To scale the force per unit volume to the order of 10^3 N/m^3, a voltage modulating scaling factor orof 10^{-11} is multiplied to the plasma force equation Eq. 3 and the sign of y-direction or normal directional force was adjusted to act into the plane of the airfoil.

III. Numerical Validation

Our baseline case of flow over the oscillating NACA 0012 airfoil without any plasma actuation is compared with the experimental data of Lee and Gerontakos[9]. The experimental results available were ensemble averaged over a large number of oscillations ranging from 100 to 150. Running such long simulations can be computationally very expensive. So, to validate our case, we ran two simulations of 21 cycles each and time averaged the lift against the angle of attack curve (C_L-α curve) using Eq. (9).

$$\bar{C}_L = \frac{\sum_{n=1}^{T}\sum_{m=1}^{P} C_L(t)}{T} \tag{9}$$

Here, $\bar{C}_L$ is the time averaged mean of all the cycles, $C_L(t)$ is the lift for during a cycle at any instant of time, T is the total number of time steps in a cycle and P is the total number of cycles in a simulation. The results are shown in Fig. 3. (a).

Subsequently, we calculated the standard deviations of lift values for each cycle with the overall time averaged mean of all the cycles through Eq. 10. As shown by Fig 3. (c), we found that except occasional aberrations, standard deviation ($\sigma_p(C_{L_p})$) for a cycle was minimized after the 5th cycle.

$$\sigma_p\left(C_{L_p}\right) = \sqrt{\frac{\sum_{n=1}^{T}\left(C_L - \bar{C}_L\right)}{T}} \tag{10}$$

Due to the loss of original experimental data, the lift against angle of attack (C_L-α) and drag against angle of attack (C_D-α) curves shown here for experiment are an approximate representation of the actual curves obtained by digitizing the plots in the paper by Lee and Geronatkos[1]. The overall trend of the curves obtained from our simulations seems to match that of the experiment although we have slighted over-predicted the drag in our numerical simulations.

Before discussing the physics of the flow, it is important to discuss the argument presented by Wang et. al[23]. The fluid particles in immediate contact with the airfoil wall would possess the same local velocity of the airfoil wall and hence at any point of time, strictly speaking, fully attached flow cannot be possible. There always exists

instantaneous streamlines either generating or ending at the airfoil surface. However, as this separation layer is very thin, it does not affect the flow field and may be ignored[23].

The airfoil starts with an initial angle of attack of 10° and goes up to 25° during the upstroke and there exists a fair agreement between the two lift curves between angles 15° to 24°, which is the important period with the occurrence of dynamic stall. As shown in Fig. 4(b), up to about 14°, the flow remains attached except at the trailing edge before a tiny Laminar Separation Bubble (LSB) is formed at about 14.5° as plotted in Fig. 4(c), which is onset flow reversal and a turbulent boundary layer.

As the airfoil continues to pitch up, the turbulence intensity is increased, the region of flow separation grows in size and the flow over the suction surface becomes fully separated as this LSB causes another pair of counter rotating eddies upstream of it. At around 21°, the turbulent boundary layer breaks down, forming the Leading Edge Vortex (LEV), as shown in Fig. 4(e). This LEV grows in size as the angle of attack is increased and is convected towards the trailing edge. Looking at the drag curve, it can be seen that drag increases steadily as the size of the separation region increases and there is a steeper increase in drag as the LEV is formed and again falls sharply as the LEV is shed. From Fig. 3(g) it can be seen that just before shedding at about 24°, the LEV has enveloped around 90% of the airfoil surface, where the highest value of lift is obtained. The time averaged peak value of lift obtained by from our simulations was 2.396 (Max: 2.45, Min 2.28) which occurred at an angle of 23.57° whereas the peak value of lift obtained from experiment was 2.44 at an angle of 24.7°. Fig. 4(i) shows that after the LEV is shed; the airfoil is stalled for a brief period until a weaker secondary vortex is formed around 24.53° which causes a sharp rise in lift. This rise however is more than that predicted from experiment and may be due to 2d modeling of the turbulence which is a 3d phenomenon and a 3d environment might have dissipated this weaker vortex.

The effect of this vortex is also reflected in the drag curve which also shows a smaller peak at that time. As the airfoil continues to pitch down, there is a large recirculation region formed over the suction surface as shown in Fig. 4(l) which causes the lift curve to shift upward again and causes another disparity between our solutions and the validation case. Flow remains separated and numerous eddies continue to be formed and shed from until flow reattaches except at the trailing edge at around 1.8°. These waves of disturbance as can be in Fig. 3(l)-3(o) causes the curve to have an oscillatory nature during the downstroke. The presence of this turbulence can again be attributed to the 2d nature of the flow and needs to be compared with a 3d numerical simulation. The curves from our present simulation and experiment match at the lowest angle of attack of attack -5°. However, as the airfoil pitches up again, our model slightly over-predicts lift compared to the validation data, which may due to the effects of hysteresis and the presence of small residual eddies in the flow over the suction surface. The curve for the moment coefficient is presented in the following sections without a comparison with the validation data as it reported values of the order 10^{-2}. Our values were of the order of 10^{-1} and matched with known values in literature[18, 22].

IV. Results

To study the effects of plasma actuation on the oscillating airfoil, we have studied several cases to determine the best strategy for flow control and enhancement of airfoil performance. As discussed earlier, we have tested different locations of placement of the plasma actuator, its orientation and the effect of pulsed actuation

We first discuss the results for steady actuation, wherein the plasma actuator is on continuously for the entire part of the cycle. As the standard deviation of a cycle is minimized after the 5th cycle, all data is collected from the 6th cycle onwards. Starting with the initial condition as the end of the 5th cycle, 10 cycles from 6-15 were run without plasma actuation and another 10 cycles from 16-25 were run with plasma actuation. Time averaged data of these 10 cycles each have been used as the final results of each case. Table I. provides the values of the parameters used to quantify the plasma force given by Eq. 3. The meaning of the terms has already been explained earlier. It is important to note that the results shown here for every case are theoretical predictions for the plasma force magnitude and distribution shown for that case, approximated from the force model given by Eq. 3. The magnitude of the plasma force ranged from a maximum of 8×10^3 N/m^3 at the leading edge to 15×10^3 N/m^3 at the mid-chord and trailing edge locations. The horizontal component of the force was greater in magnitude and well distributed than the normal component which had a narrower and sharper region of influence.

While we observed the effect of the actuator on events like onset of flow separation and dynamic stall, we calculated the overall change in lift, drag or moment during an oscillation cycle by Eq. 11. We time integrated the lift, drag or moment values for each case and subtracted and divided it by the time integrated values for the no-actuation case.

$$\Delta_{property} = \frac{\int C_{property(with-plasma)}(t)dt - \int C_{property(without-plasma)}(t)dt}{\int C_{property(without-plasma)}(t)dt} \tag{11}$$

Table I. Parameters chosen for the plasma force model

Parameter	Value
φ_0	7000 Volts
F_{x0}	2.6
F_{y0}	2.0
β_x	8×10^5 m^{-2}
β_y	10^7 m^{-2}
y_0	Height of airfoil surface

A. Plasma Actuator placed at the Leading Edge

For most part of the cycle, the suction side of the leading edge is oriented against the direction of the incoming flow and it was hoped that placing a plasma actuator at this location would help in smooth transitioning and attachment of the flow as it flow over the leading edge. Thus, the region of influence for the actuator was chosen to be from from x=0 m to x=0.015 m extending on its suction surface. In the normal direction, it extended 2cm outward following the curvature of the surface at every point. The midpoint between the RF and grounded electrode (x_0) was chosen to be 0.005m. This was done assuming an actuator length of 1cm and the region of influence was chosen to be an addition 0.5cm long in order to fade out the force. The distribution and location of the force is shown in Fig. 4.

The horizontal and vertical forces are applied in the normal and tangential directions to the surface of the airfoil respectively as shown in Fig. 1. From Fig.5, it can be inferred that the plasma actuator creates a very concentrated and localized body force which imparts momentum to the fluid.

1. Steady Co-flow actuation at the leading edge

Fig. 6 shows the effect of steady co-flow actuation at the leading edge. With the actuator on, the lift can be seen to have improved for most part of the cycle. The primary observable effect of the actuator was suppressing the flow separation and promoting attachment by providing a favorable pressure gradient. There was a 27.52% increase in lift and 12.45% reduction in drag when integrated over the entire cycle compared to the no actuation case.

From the initial angle of attack of 10°, up to about 20° during the downstroke, there is a slight improvement in lift. When there was no actuation, FIG. 4(b) shows how the Laminar Separation Bubble starts to form near 14.5° and flow started to separate at higher angles of attack. However, as can be seen from FIG. 7(a)-(c), plasma actuation has delayed flow separation and symptoms of flow reversal. Fig. 7(d) shows that the onset of flow reversal at the leading edge occurred only around 20.8°. This delayed flow separation and attached flow creates greater lift and reduced drag during the upstroke beyond 15° as evident from Fig. 6(a) and 6(b).

It can also be seen from the lift curves Fig. 6(a) and 6(d), that the actuator has caused a delay of dynamic stall from 23.57° to 24.64°. The peak value of lift however, was almost the same in both the cases. When the actuator was turned on C_{Lmax} was 2.406, while it was 2.396 when the actuator was turned off. At the same time, the actuator has delayed the moment stall but has not been able to reduce the large negative peak of the coefficient of moment. The maximum drag experienced during the oscillation cycle has actually risen after plasma actuation, but the nature of peak has changed from a flatter to a sharper.

During the downstroke, the actuator proved to be highly effective at angles of attack below 15°. When comparing with the no actuation case, Fig. 4(k)-4(l) shows that even at lower angles of attack during the pitch down motion, there is separated flow and presence of turbulent eddies over the suction surface. Fig. 7(k) shows that at 16°, flow has started to reattach at the leading edge while there is some residual turbulence near the mid chord region. It is around the same time that by promoting earlier reattachment, the plasma actuators has been able to significantly improve the lift and moment values compared to the no actuation case. Fig. 7(l) shows a much smaller separation region compared to Fig. 4(l). Fig. 4(m) shows that even at 5.5°, flow has not reattached completely, while in comparison Fig. 7(m)-(n) show attached flow except near the trailing edge at a significantly higher angle of 9.21° and fully attached flow at 5°. The minimum value of lift at the lowest angle of attack of -5° increased from -0.247 to 0.051 and thus, there is no negative lift during the oscillation cycle.

2. Steady Counter-flow actuation at the leading edge

Counter-flow actuation offers adverse pressure gradients which triggers earlier flow separation and transition to turbulence. It has been also said that this helps to break down the larger vertical structures into smaller structures which better attach to the surface. However, in contrast to the benefits associated with co-flow actuation at the leading edge, counter-flow actuation was actually found to be detrimental to airfoil performance. When integrated over the entire cycle, lift decreased by 8.34% and drag increased by 15.05%. Counter flow actuation created adverse pressure gradients that caused earlier flow separation and turbulence, leading to reduced airfoil performance. The effects are shown in Fig. 8.Flow separation occurred very early during the oscillation cycle. As shown in Fig. 9(a), just above 10° angle of attack, a tiny bubble can be observed at the leading edge. Fig. 8(a) shows that from 10° to 14°, the two curves almost overlap but around 14°, the curve for plasma on lifts off as the bubble grows to form the LEV, as shown in Fig. 9(b) and eventually causes a premature dynamic stall at 21.85°, compared to 23.57° in the no actuation case.

The peak value of lift C_{Lmax} obtained was 2.437, which is marginally higher than the C_{Lmax} of 2.396, obtained when the actuator was turned off. The direction of force due to the counter-flow arrangement favored the counter-clockwise rotating LEV and increased its strength, resulting in a higher value of peak lift. The continued presence of a large separation region has also caused the airfoil to experience higher drag and moments as shown in Fig. 8(b) and 8(c). During the downstroke, flow remains unattached even at very lower angles of attack as shown in Fig. 9(m)-(o). While the earlier attachment of the flow in the co-flow case had caused the lift curve to shift upwards below the angle of attack of 15°, in this case, due to separated and turbulent flow, the lift curve shifted downwards until about 0°, when flow finally reattached. Fig. 8(d) shows the oscillatory nature of the time dependent lift curve due to the presence of tiny eddies and turbulence over the airfoil surface. This oscillatory behavior is generally gets filtered in the time averaged curves.

B. Plasma actuator placed at the mid-chord location

The vortices created at the leading edge tend to grow and convect at downstream until it sheds at the trailing edge. As such, it might be interesting to observe the effect of a plasma actuator placed around the mid chord region, which might attach the flow or break down the vortices depending on whether the plasma actuator is in the co-flow or counter flow arrangement. The region of influence was chosen to be 2cm long in the chordwise direction from x=0.065m to x=0.085m.

The midpoint of the dielectric surface was exactly the midpoint of the airfoil x=0.075m. Once again, it was assumed that the actuator was 1cm long, but an additional 1cm was chosen to fade out the force. The length of the extended zone was chosen to be larger than that at the leading edge in due to the flatter profile of the airfoil in this zone. This however also resulted in a horizontal force magnitude being larger than the horizontal force at the leading edge. The force distributions are shown in Fig. 10(a) and 10(b).

1. Steady Co-flow Actuation at mid-chord

This case was found to be beneficial for enhancement of lift and delay of dynamic stall while there was not much of a benefit in terms of drag except at lower angles of attack during the downstroke. The characteristic curves are shown in Fig. 11. Overall, there was 29.23% increase in lift and 1.715% decrease in drag, while the lift to drag ratio increased by 18.97% integrated over the entire cycle. The sequence of events during the oscillation cycle is shown in Fig. 12.

When the airfoil starts pitching up from the initial angle of attack of 10°, flow remains attached at the leading edge for a longer duration. Compared to the no actuation case, when the onset of flow reversal occurs around 14.5° with the occurrence of a laminar separation bubble, it was delayed to 17.74° in this case, when a number of small bubbles were formed. The LEV formed at slight delay of 21.76°, after which it convected faster to the location in between the mid chord and trailing edge rather rapidly, where it grew in size and remained attached for a longer duration. Dynamic stall was thus delayed from the usual 23.57° to 24.29°. Fig. 11(d) shows the shift of the curve towards the right during dynamic stall, when the plasma actuator was turned on. In addition to the delay in dynamic stall, there was also a rise in the peak value of lift (C_{Lmax}) to 2.605 compared to 2.396 in the no actuation case. Fig. 12(e) shows the LEV at its maximum strength and its position, shifted downstream of the actuator.

However, there was higher moment at angles higher than 15°. Figs. 11(b) and 11(c) show that the co-flow actuator placed at the mid chord was not that effective in terms of drag or moment at very high angle of attack. In fact, peak drag C_{Dmax} and peak moment C_{Mmax} was 1.195 and -1.127 respectively compared to 1.063 and -1.04 respectively when there was no actuator present.

As the airfoil pitched down, it was once again seen that the actuator was highly effective below 15°. By providing a favorable pressure gradient and also by injecting momentum into the recirculation region it helped to

reduce the size of the separation region, allowed earlier reattachment of the flow and reduced the formation of turbulent eddies at the trailing edge which are adverse to airfoil performance. A combination of all these factors helped the airfoil generate greater lift while experiencing lesser drag and moment at lower angles of attack during the downstroke, resulting in an overall enhancement of performance.

Compared to the leading edge actuation case, this case can be said to be less effective as it is able to address the flow that has already separated at the leading edge and works to mitigate the size of the recirculation zone in the latter half of the airfoil. The leading edge actuator works better at keeping the flow attached from the onset and as a result the separation zone over the entire airfoil surface is much reduced, which helps to reduce the drag. While we predict a higher value of lift in this case, it must also be kept in mind that we use a slightly larger actuator with a higher force density, which further enhanced lift by injecting greater momentum into the low pressure region.

2. Steady Counter-flow Actuation at mid-chord

The counter-flow arrangement at the mid chord greatly limited the performance of the airfoil. It caused massive flow separation over the entire airfoil which severely altered the flow physics and normal sequence of events. It reduced the lift by as much as 47.94%, increased drag by 8.51% and the lift to drag ratio was reduced by 52.92%.

Right after the start of the cycle, the resistance to the flow due to the presence of the actuator caused the flow to separate past the leading edge. As the airfoil pitched up, the formation of the laminar separation bubble and subsequently, the leading edge vortex was suppressed even as separation region downstream of the actuator grew in size. Even as the LEV was formed at a higher angle of attack, this huge counter rotating vortex extending beyond the mid chord prevented the LEV from growing or convecting downstream beyond the mid chord. Thus, unlike the usual scenario, there was no steep increase in lift and the lift curve for the airfoil with plasma turned on remained flat and always below the lift curve for the airfoil without plasma actuation. There was not much of a significant negative effect on drag except that there was no peak during higher angles of attack, as the LEV had been suppressed. During the downstroke, it can be seen from Fig. 14(m)-(p), that the huge separated flow region persisted throughout and even at the lowest angle of -5°.

C. Plasma actuator placed at the Trailing edge

By observing flows past the oscillating airfoil, it could be noticed that the trailing edge experiences a considerable amount of turbulence, with large separation layers and turbulent eddies. In addition, the vortices formed at the leading edge are convected downstream and shed at the trailing edge. By reducing the thickness of the separation layer and turbulent eddies along with attachment of the large vortices for a longer duration may lead to higher lift.

A plasma actuator was placed at about the 2/3rd chord length location to test its capabilities in addressing these. Once again, due to flatter profile of the airfoil at the trailing edge, the region of influence was chosen to extend 2cm from x=0.095m to x=0.115m. The midpoint location (x_0) was x=0.105m. The horizontal component of the force was same as that at the mid chord and greater than that at the leading edge.

1. Steady Co-flow actuation at the trailing edge

This approach offered 22.11% increase in lift, 1.90% reduction in drag and 15.53% improvement of the lift to drag ratio when integrated over the entire cycle. It was not able to delay dynamic stall but was able to increase the peak value of lift and generate greater lift for most part of the cycle.

The sequence of events is shown in Fig. 17. The flow at the leading edge develops normally and forms the laminar separation bubble and leading edge vortex around 14.5° and 21° respectively, as it normally occurs without any plasma actuation. Meanwhile, it can be seen from Fig. 17(c), that the thickness of the separation layer at the trailing edge is less than that observed in the baseline case shown in Fig. 4(c). The dotted circle in Fig. 17(d) shows he effect of the actuator which keeps the flow attached at the trailing edge. Even as the leading edge vortex grows in size and convects downstream, the initial effect of the actuator was to keep the LEV from growing further and allow the freestream the travel smoothly over the trailing edge.

This attachment of the flow at the trailing edge results in slightly higher lift and lower drag. As the airfoil continues to pitch up, the LEV grows to envelop most of the suction surface and is held in this position for a longer duration. It is interesting to note that peak lift C_{Lmax} of 2.482 was obtained at the same angle of 23.57°, after which there was a brief and gradual drop in lift up to 24.3° and sharp fall in lift thereafter. This stronger vortex also results in a higher peak in drag and moment. Maximum Drag (C_{Dmax}) was 1.138 while peak moment (C_{Mmax}) was -1.04.

The characteristic width of the peaks for drag and moment remained the same while the leading edge case, where they were narrowed and delayed.

As the airfoil pitches down, it can be seen again in Fig. 17(i), that the actuator favors smooth flow of the streamlines over the trailing edge with a very narrow separation layer. This offers resistance to the convection of the weaker secondary vortex towards the trailing edge and it is eventually split into two counter rotating vortices which are shed off later around 20°. Due to this weakening of the vortex and formation of two counter rotating vortices, Fig. 16(a) and Fig. 16(d) shows, that in the entire cycle, only during this regime 24° to 20° of the downstroke we have lower lift than the baseline case. In addition to lower lift there was also greater drag in this regime.

At angles below 15°, lift increased again to consistently higher values, once again reinstating the effectiveness of co-flow approach at lower angle of attack during the downstroke. Fig. 17(m) shows how the injection of momentum into the separation region causes the trailing edge to experience lesser turbulence, while the eddies formed at the leading edge are suppressed and resisted from growing. This promoted earlier reattachment of the flow as the airfoil kept pitching down to lower angles of attack.

Compared to leading edge and mid chord actuation, this was to be the least effective location. While it was effective in serving its purpose of reducing the thickness of the separation layer and mitigation of turbulent eddies formed at the trailing edge, overall it did not prove as effective as the other two cases. The overall improvement of lift was less than the other two cases of co-flow actuation, along with not much of a significant effect on drag or moment. The persistence of separation zones upstream of the actuator accounts for this difference.

2. Steady Counter flow actuation at the Trailing edge

Like the other cases of counter flow actuation, this case also proved to be detrimental to airfoil performance. There was a 31.19% reduction in lift and 8.95% reduction in drag. The aerodynamic coefficients are compared in Fig. 18(a)-18((d).

The actuator forces the flow to remain separated throughout the cycle, right from the beginning of the cycle as shown in Fig. 19(a). Working in a manner opposite to that actuator in co-flow arrangement, it resists the growth of the leading edge vortex and initiates its earlier shedding from a slightly upstream position, as shown in Fig. 19(h). After the LEV is shed, there is a period during which flow is sucked off the pressure side of the trailing edge. The actuator provides aids this suction due to its arrangement and force direction resulting in the creation of a trailing edge vortex as shown in Fig. 19(i) which sustains and grows at that location affecting a temporary boost in lift just before 25°.

As the airfoil starts pitching down, the weaker secondary vortex at the leading edge seen in Fig. 19(i) grows and convects downwards before finally shedding off the trailing edge. Even as the airfoils pitches down to lower angles of attack, the trailing edge actuator keeps the flow separated with a local recirculation zone around it as shown in Fig. 19(m). This also forces the flow past the leading to pass over this recirculation zone, resulting in the spreading of the separation zone up to the leading edge. As a result, there is less lift and increased drag. At an almost flat angle of attack as shown in Fig. 19(o)-(n), the flow at the leading edge reattaches but remains separated at the trailing edge.

D. Special Cases

In addition to the effect of location and arrangement of the plasma actuator, we tested the effect of pulsed actuation and the effect of reversing the direction of the normal component of the force as shown in Fig. 20. Since, the actuator placed at the leading edge seemed to provide the best results, we chose to test these cases with the actuator placed at the leading edge.

1. Effect of Pulsed Actuation

Two cases were tested for pulsed actuation with varied Strouhal numbers and the corresponding forcing frequency. The Strouhal number is given by $St=fc/U_\infty$ where f is the actuator forcing frequency, c is the chord length and U_∞ is the freestream velocity. We considered two cases with $St=1$ and $St=0.267$, with corresponding forcing frequencies being 93.33 Hz and 25 Hz respectively. In comparison the physical oscillation frequency of the airfoil was 2.97 Hz. The duty cycle for the unsteady actuation was chosen to be 10% and thus the actuator was activated for only 10% of the time. Compared to steady actuation, this implies a reduction of input power by 90%. While steady actuation provides continuous injection of momentum, pulsed actuation imparts short bursts of impulses into the fluid. From a time scale perspective, the 93.3 Hz actuation meant that for one duty cycle of 10 ms, the actuator was turned on for 1 ms and turned off for 9ms. For the frequency of 25 Hz frequency, it corresponded to 4 ms on and 36 ms off. One complete oscillation of the airfoil took about 336 ms.

Fig. 21(a)-(c) shows the effect of pulsed actuation. 25 Hz unsteady actuation was found to be more effective than the 93.3Hz actuation case, but nevertheless both the cases were found to be less effective than the steady actuation case. With the 25 Hz pulse frequency, there was 14.10% overall increase in lift, 2.81% reduction in drag and 7.10% improvement of the lift to drag ratio. For 93.3 Hz actuation frequency, there was 7.23% increase in lift, 5.38% reduction in drag and 5.81% improvement of the lift to drag ratio.

During the upstroke, there was not much observable increase in lift or decrease in drag for pulsed actuation compared to the no-actuation case. There was a slight delay in dynamic stall for both the cases of pulsed actuation and the peak value of lift for the 93.3 Hz case was marginally lower than the no actuation case. However, the peak value of lift for the 25 Hz case was $C_{Lmax} = 2.424$ which was greater than the $C_{Lmax} = 2.402$ offered by steady actuation. At the same time though, the drag in the 25Hz case was slightly higher beyond 18° than the steady actuation or no actuation case. Compared to the steady actuation case, the drag or moment stall had not been delayed or shortened by pulsed actuation, as can be seen in Fig. 21(b)-(c).

The highlight of co-flow actuation in the all the cases so far has been the earlier reattachment of the flow during the downstroke which causes significant improvement of lift and reduction of drag. In this situation, the 25Hz pulsed actuator generated higher lift than the steady actuator in between angles 16.5° to about 8.5°, whereas in comparison the 93.3 Hz actuator was not able to generate as much lift and stayed below the other two curves. In Fig. 21(b), it can be seen that the steady actuator has always helped reduce more drag during the downstroke compared to pulsed actuators.

Thus, it can be said that while unsteady actuation can be beneficial in terms of reduction of input power, our results shown that steady actuation strategy helps greater enhance airfoil performance than unsteady actuation.

2. Effect of reversing the normal component of the plasma force

While co-flow actuation has already been tested where the horizontal component of the plasma force acted in the direction opposite to the freestream, we chose to test one case with the normal component of the plasma force acting in the direction outward to the airfoil surface as shown in Fig. 20. Fig. 21(d)-(f) shows the characteristics curves for this case. The overall improvement of lift was considerably lower at only 3.77%, but surprisingly, there was a high reduction in drag of 11.60%. Dynamic stall occurred at almost the same angle as the no actuation case but the maximum value of lift was raised significantly to 2.537, second only to the mid chord co-flow actuation case. However, there was also a major rise in moment during dynamic stall which reduces the desirability of this case. Also, during the downstroke, the separation zone thickness did not reduce with the fluid being pushed outward from the airfoil at the leading edge, which led to lower values of lift generated.

V. Summary and Discussion

This paper presents a theoretical prediction of the influence of plasma actuation on the performance of an oscillating NACA 0012 airfoil in deep dynamic stall. Several strategies were investigated to test the effectiveness of the actuator was based on its arrangement and location along the airfoil surface as well as continuous and pulsed operation. A brief summary of all these cases have been presented in Table II. While co-flow actuation proved to be beneficial in enhancing lift, counter flow actuation of an airfoil oscillating in deep dynamic stall was found to be drastic to its performance. The nature of the flow past an airfoil oscillating in deep dynamic stall is in itself very complex and characterized by massive flow separation and turbulence. Introducing greater separation and turbulence using counter-flow actuation naturally depreciated airfoil performance considerably. Pulsed actuation at a lower frequency and 10% duty cycle seemed to be more effective than an actuator with higher frequency but overall proved to be less effective in enhancing airfoil performance than steady actuation.

The actuator placed in co-flow arrangement at the mid chord and trailing edge location were found to be beneficial in terms of lift but did not improve drag or moment characteristics. Mid chord based actuation however resulted in the maximum peak value of lift. Just before the LEV is shed, it enveloped around 90% of the airfoil suction surface and the injection of momentum at the mid chord location resulted in a stronger vortex. Both the trailing edge actuator and the mid chord actuator effectively worked by reducing the span of the separation region downstream of it and injecting momentum into the low pressure regions. However, as the flow starts separating at the leading edge, the zone between the leading edge and the actuator remained separated and hence improvement in lift was limited and related to the length of the airfoil downstream of the actuator.

Table II. Comparative summary of all cases

Case Description	Dynamic Stall Angle (α_{ds})	C_{Lmax}	C_{Dmax}	C_{Mmax}	Overall Δ_{Lift}	Overall Δ_{Drag}
Without plasma actuation	23.57°	2.396	1.063	-1.04	---	---
Leading Edge Co-flow	24.64°	2.402	1.126	-1.049	+27.52%	-12.45%
Leading Edge Counter-Flow	21.85°	2.437	1.143	-1.141	-8.34%	+15.05%
Mid Chord Co-Flow	24.29°	2.605	1.195	-1.127	+29.23%	-1.715%
Mid Chord Counter-Flow	---	1.264	0.694	-1.04	-47.94%	-8.519%
Trailing Edge Co-Flow	23.57°	2.482	1.138	-1.135	+22.11%	-1.90%
Trailing Edge Counter-Flow	21°	1.846	0.854	-0.858	-31.19%	-8.95%
Leading Edge Pulsed f = 93.3 Hz	24°	2.36	1.113	-1.078	+7.23%	-5.38%
Leading Edge Pulsed f = 25 Hz	24.11°	2.424	1.126	-1.069	+14.10%	-2.81%
Leading Edge Reversed N-Force	23.68°	2.537	1.068	-1.188	+3.77%	-11.60%

It is prominent from our discussion above and the summary of results in Table II, that steady co-flow actuation at the leading edge was the best strategy for plasma based flow control in this scenario. By facilitating better attachment of the flow past the leading edge, it was more effective in reducing the thickness of the separation zone and low pressure regions that are normally formed. By promoting attachment of the flow from the leading edge itself, it was able to reduce turbulence for a greater part of the airfoil compared to the actuator placed at the mid chord and trailing edge. Fluid velocities over the airfoil were increased which aided greater generation of lift. Moreover, at higher angles of attack, the leading edge actuator caused the LEV to be sustained for a longer duration, thereby delaying dynamic stall. Delay of dynamic stall has several advantages, as it increases the operating angle of attack and allows aerial vehicles like rotorcrafts to operate at greater velocities. In addition, the 12.45% reduction in drag associated with leading edge actuation is the maximum obtained for any case. A combination of these benefits would make leading edge steady plasma actuation a fitting strategy for enhancement of airfoil lifting and drag characteristics.

VI. Conclusion and Future Work

Plasma based flow control provides motivation for being used as an alternative flow control device. Our results show that there can be a significant improvement of lift associated with the use of plasma based flow control devices and as such holds considerable promise for the future. Although, these predictions rely on a two dimensional model and hence are limited in their accuracy, they do provide a foundation and motivation for experiments of similar nature as well as development of a 3D model with the availability of improved computational resources. As most of the turbulent phenomenon associated with such flows is of 3d nature, such a model would help to improve these results. A 3D environment would also provide the possibility of adding degrees of freedom. MAVs and rotorcraft wings are also known for their flexible beam type behavior and our present results provide a platform for testing of plasma based devices in such fluid structure interaction problems.

REFERENCES

[1]Combes. S. A., and T. L. Daniel. "Flexural stiffness in insect wings. I. Scaling and the influence of wing venation," *J. Exp. Biol*. **206**, 2979–2987 (2003a)

[2]Combes. S. A., and T. L. Daniel. "Flexural stiffness in insect wings. II. Spatial distribution and dynamic wing bending," *J. Exp. Biol*. **206**, 2989–2997 (2003b)

[3]Mountcastle. A.M., Daniel. T.L., "Aerodynamic and functional consequences of wing compliance," *Experiments in Fluids.* **46**(5), 873-882 (2009)

[4]Ashraf. M.A., Lai. J.C.S. and Young. J., "Numerical Analysis of Flapping Wing Aerodynamics," *16th Australasian Fluid Mechanics Conference*, Crown Plaza, Gold Coast, Australia 2-7 December 2007.

[5]Sane S.P., "The aerodynamics of insect flight," *J. Exp. Biol*. **206**, pp. 4191-4208 (2003)

[6]Ellington. C.P, Berg. C.V.D, Willmott. A.P., Thomas. T.L.R., "Leading edge Vortices in insect flight," *Nature*, Vol. 384. No. 19, 1996, pp. 626-630.

[7]Ellington. C.P., "The Novel Aerodynamics of insect flight: Applications to Micro Air Vehicles," *J. Exp. Biol*, **202**, 3439–3448 (1999)

[8]Zbikowski. R., "On aerodynamic modelling of an insect-like flapping wing in hover for micro air vehicles," *Phil. Trans. R. Soc. Lond. A.* **360**, 273-290 (2002)

[9]Lee. T and Gerontakos. P., "Investigation of flow over an oscillating airfoil," *Journal of Fluid Mechanics,* **512**, 313-341 (2004)

[10]Wu. P., Stanford. B.K., Sallstrom. E., Ukeiley. L., Ifju. P.,"Structural dynamics and aerodynamics measurements of biologically inspired flexible flapping wings," *Bioinsp. Biomim*. **6** (2011)

[11]Ifju. P., Jenkins. D., Ettinger. S., Lian. Y., Shyy. W., and Waszak. R. M., "Flexible-Wing-Based Micro Air Vehicles," AIAA Paper 2002-0705. Reno, NV, January 2002.

[12]Ganguli. R., Gorb. S., Lehmann F.O., Mukherjee S., Mukherjee. S., "Experimental and Numerical Study of Calliphora Wing Structure," *Experimental Mechanics*. **50**(8) 1183-1197 (2010)

[13]Jacob. D.J., "On the Fluid Dynamics of Adaptive airfoils," Proceedings of 1998 ASME International Mechanical Engineering Congress and Exposition November 15-20, 1998, Anaheim, CA, USA

[14]Cox. A., Monopoli. D., Cveticanin D., Goldfarb. M., Garcia. E., "The Development of Elastodynamic Components for Piezoelectrically Actuated Flapping Micro-air Vehicles," Journal of Intelligent Material Systems and Structures, **13**, 611-615 (2002)

[15]Lian, Y., Steen, J., Trygg-Wilander, M., and Shyy, W., "Low Reynolds Number Turbulent Flows around a Dynamically Shaped Airfoil," *Computers and Fluids*, **32**, 287-303 (2003)

[16]Roth, J.R., Sherman, D.M., Wilkinson, S.P., "Electrohydrodynamic flow control with a glow discharge surface plasma," *AIAA Journal*,38(7),1166-1172 (2000)

[17]Corke T.C., Post M. L., Orlov D.M., "SDBD enhanced aerodynamics: concepts, optimization and applications," *Progress in Aerospace Sciences* **43**, 193-217 (2007)

[18]Singh, K.P.and Roy,S. "Simulation of an asymmetric single dielectric barrier plasma actuator", *Journal of Applied Physics*, **98**(8), 083303, 2005.

[19]Singh K.P. and S. Roy, "Physics of plasma actuator operating in atmospheric air", Applied Physics Letters, 92 (11) 111502.(2008)

[20]Jayaraman. B., Lian Y. and Shyy. W.,"Low Reynold's number flow control using Dielectric Barrier Discharge actuators," *AIAA 37th Fluid Dynamics Conference and Exhibit*, Miami, FL, 25-28 June 2007.

[21]Post. M.L. and Corke T. C., "Separation Control Using Plasma Actuators: Dynamic Stall Vortex Control on Oscillating Airfoil," *AIAA JOURNAL,* Vol. 44, No. 12, December 2006.

[22]Bowles. P., Corke. T., Matlis. E., "Stall detection on a leading edge plasma actuated pitching airfoil using onboard measurement," *AIAA 47th Aerospace Sciences Meeting and Exhibit*, Orlando, FL, January 2009.

[23]Wang. S., Ma. L., Ingham. D.B., Pourkashanian. M. and Zhi Tao., "Turbulence Modelling of Deep Dynamic Stall at Low Reynolds Number*," Proceedings of the World Congress on Engineering*, Vol. II, London, U.K, June 30 - July 2, 2010,

[24]Singh. K.P. and Roy. S., "Force Approximation for a plasma actuator operating in atmospheric air," *Journal of Applied Physics*, Vol. 103, 2008

[25]G.J. Leishman, *Principles of Helicopter Aerodynamics* (Cambridge Univ. Press, New York, 2000)

[26]Gaitonde. D.V., Visbal. M. R. and Roy. S.. "Control of Flow Past a Wing Section with Plasma-based Body Forces," *36th AIAA Plasmadynamics and Lasers Conference*, 6-9 June 2005, Toronto, Canada.

[27]Viieru. D., Tang. J., Lian. Y., Liu. H., and Shyy. W., "Flapping and Flexible Wing Aerodynamics of Low Reynolds Number Flight Vehicles," *4th AIAA Aerospace Sciences Meeting and Exhibit*, 9 - 12 January 2006, Reno, Nevada

[28]Kang. C.K., Baik. Y.S., Bernal. L., Michael. V. O. and Shyy W., "Fluid Dynamics of Pitching and Plunging Airfoils of Reynolds Number between 1×10^4 and 6×10^4," *47th AIAA Aerospace Sciences Meeting Including The New Horizons Forum and Aerospace Exposition*, Orlando, Florida, 5 - 8 January 2009

Figures

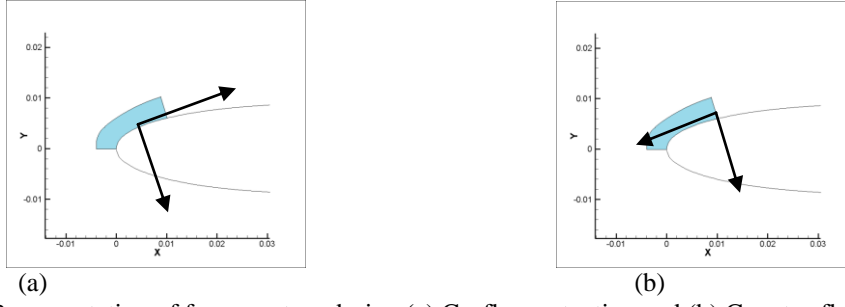(a)   (b)

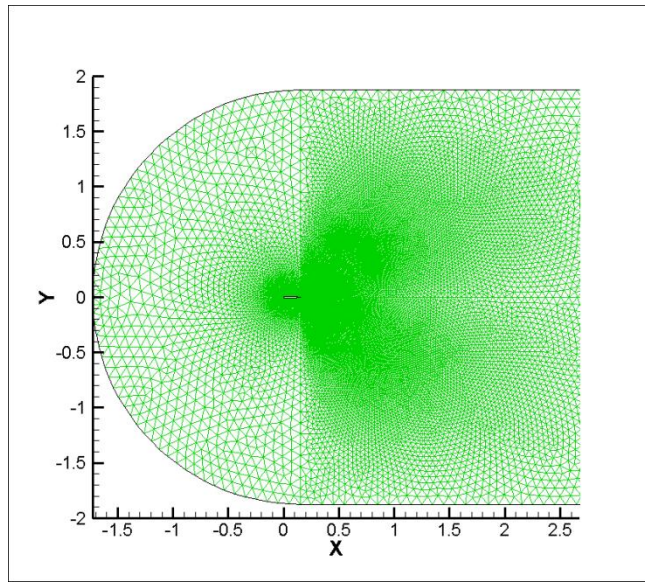FIG.1 Representation of force vectors during (a) Co-flow actuation and (b) Counter-flow actuation.
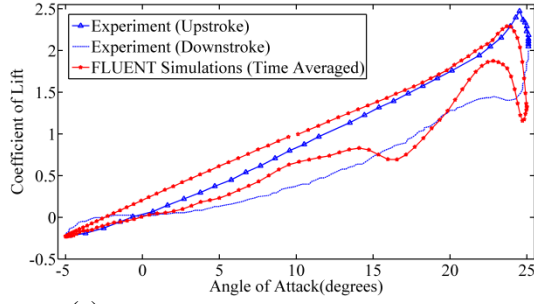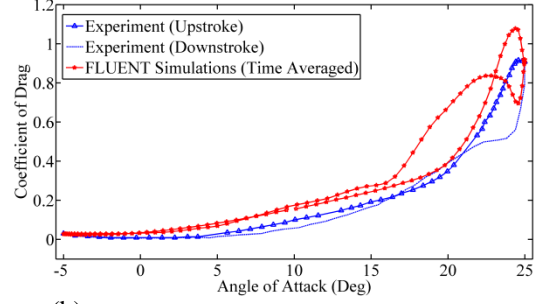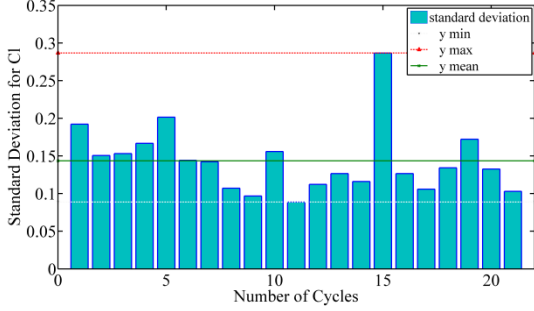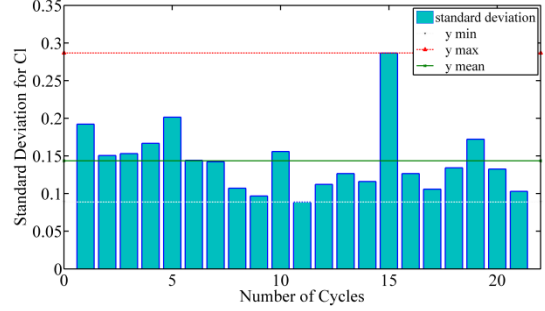

FIG. 2. Unstructured C-Type Grid used for our simulations

FIG. 3. (a) Plot comparing Fluent Simulations with experimental data for Lift against Angle of Attack (C_L Vs α) (b) Plot of Drag against Angle of Attack (C_D Vs α) (c) Standard deviation of the C_L of each cycle in a 21 cycle simulation (d) Standard deviation of C_D each cycle in a 21 cycle simulation
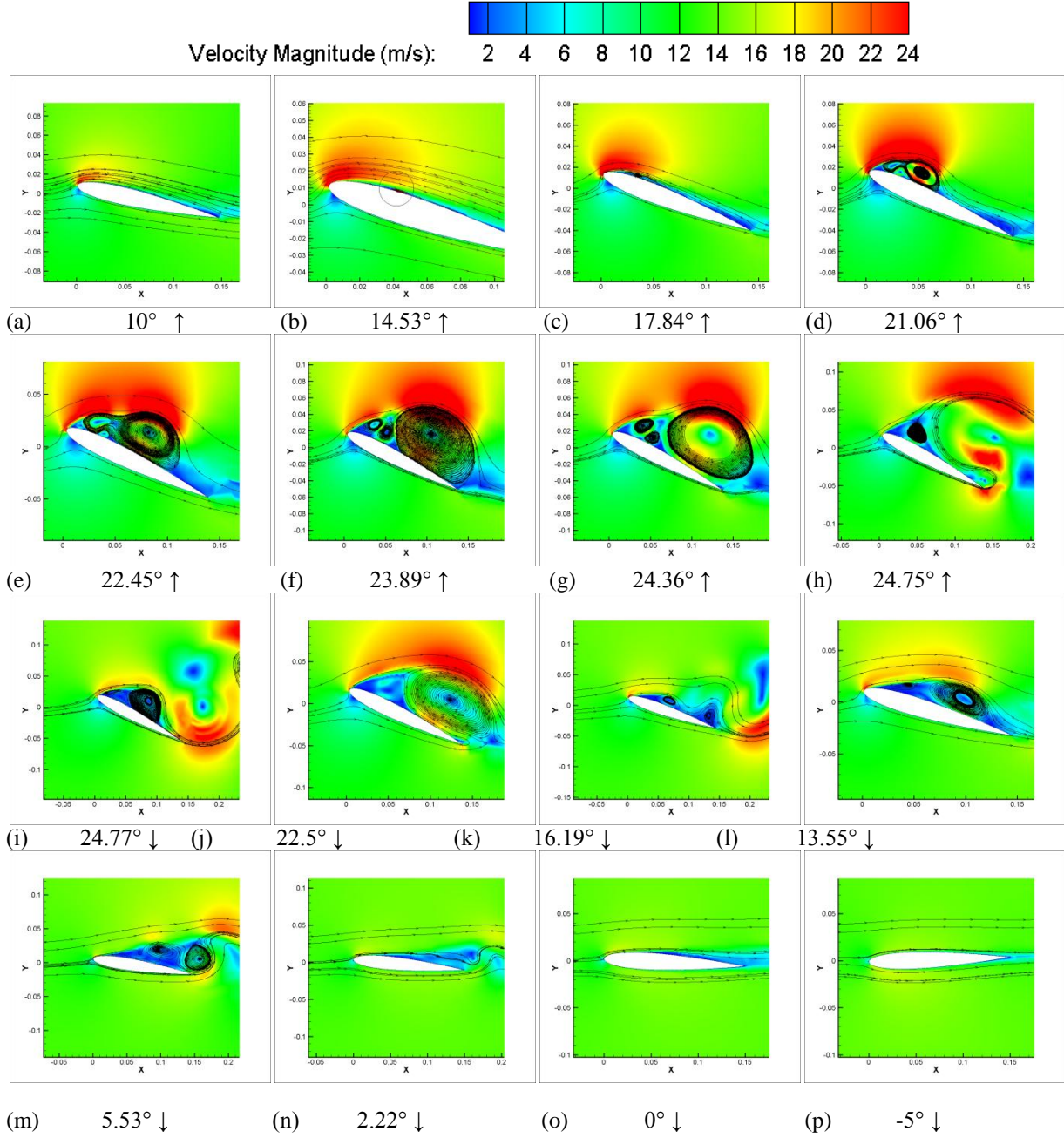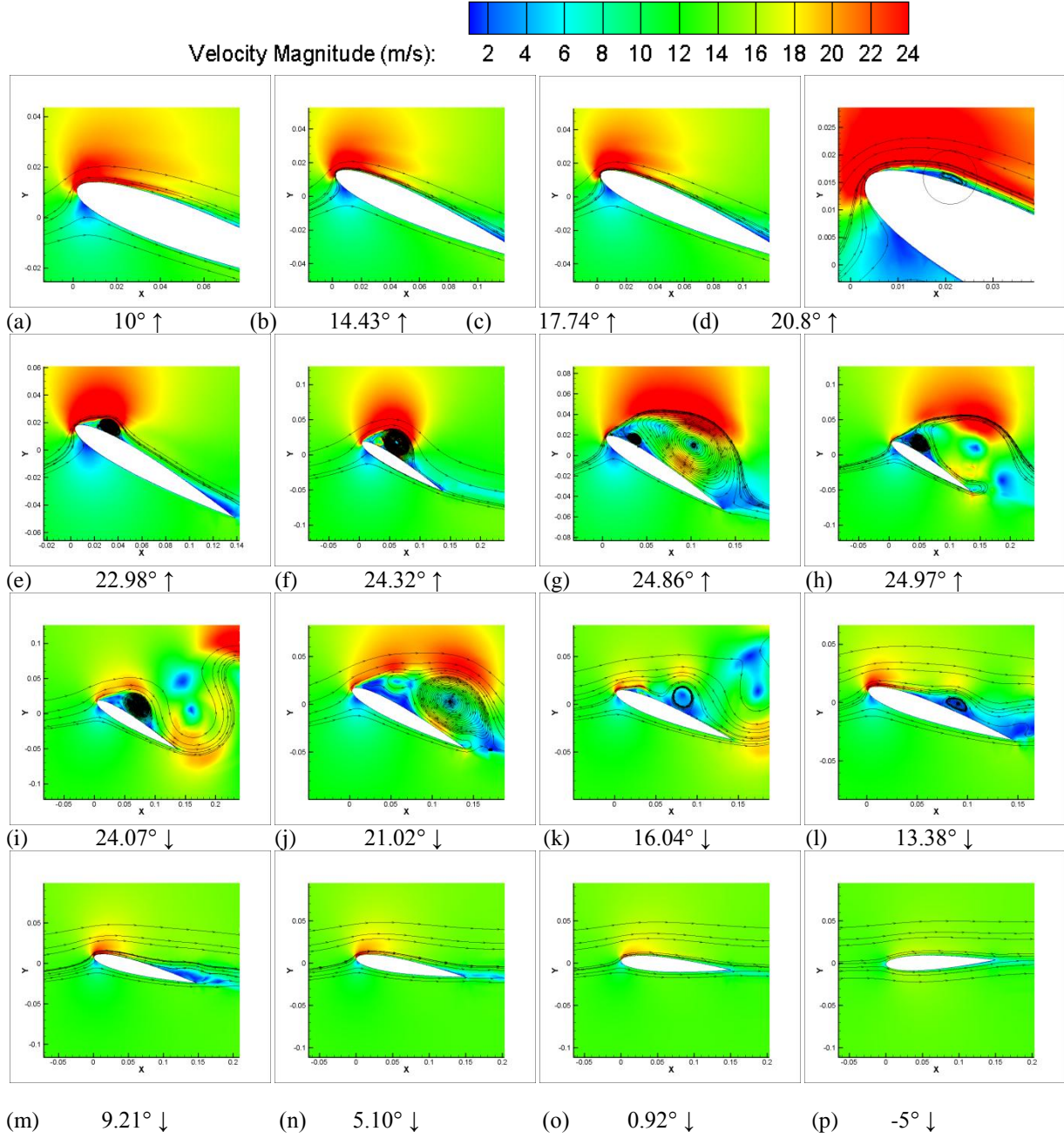
FIG. 4. Superimposed contour plots of velocity magnitude and instantaneous streamlines at different angles during an oscillation cycle. (a) Start of cycle (b) Attached flow (c) Formation of the Laminar Separation Bubble (d) Formation of the Leading Edge Vortex (LEV) (e) The LEV grows in size and is convected downstream (f) The LEV has grown to its maximum size and envelops almost 90% of the suction surface of the airfoil (g) The LEV is shed at the trailing edge (h) Stalled airfoil (i) Formation of a secondary vortex as the airfoil pitches down (j) The secondary vortex lifts off the surface (k) Turbulent eddies (l) Flow is still remains to be reattached (m) Reduction in the size of the flow separation region but eddies continue to be formed and shed off the suction surface (n) Flow beginning to reattach at the leading edge while residual eddies are shed at the trailing edge (o) Reattached flow except at the trailing edge at 0° (p) Lowest angle of attack during the oscillation cycle

(a)   (b)
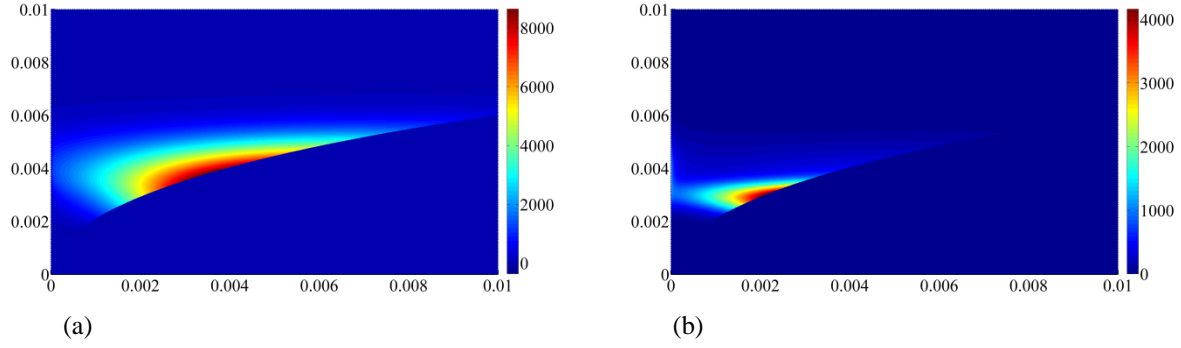
FIG. 5. Contour plots showing the location, distribution and magnitude of the force due to the plasma actuator at the leading edge (a) Horizontal Force (b) Vertical force
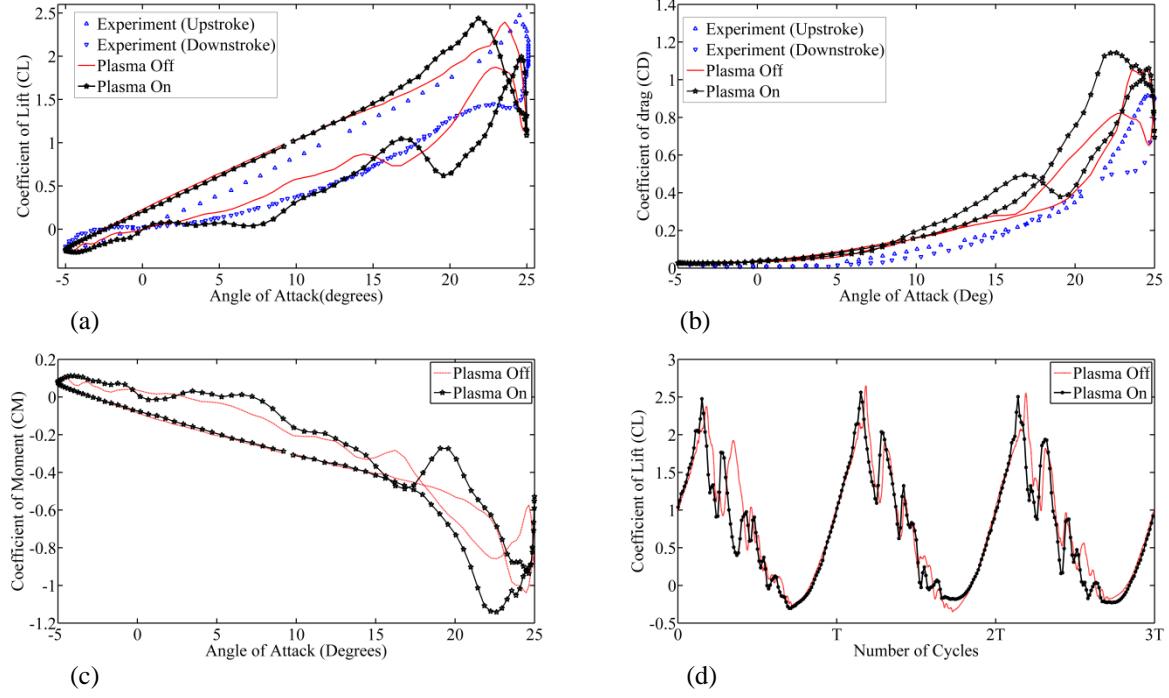

(a)   (b)

(c)   (d)
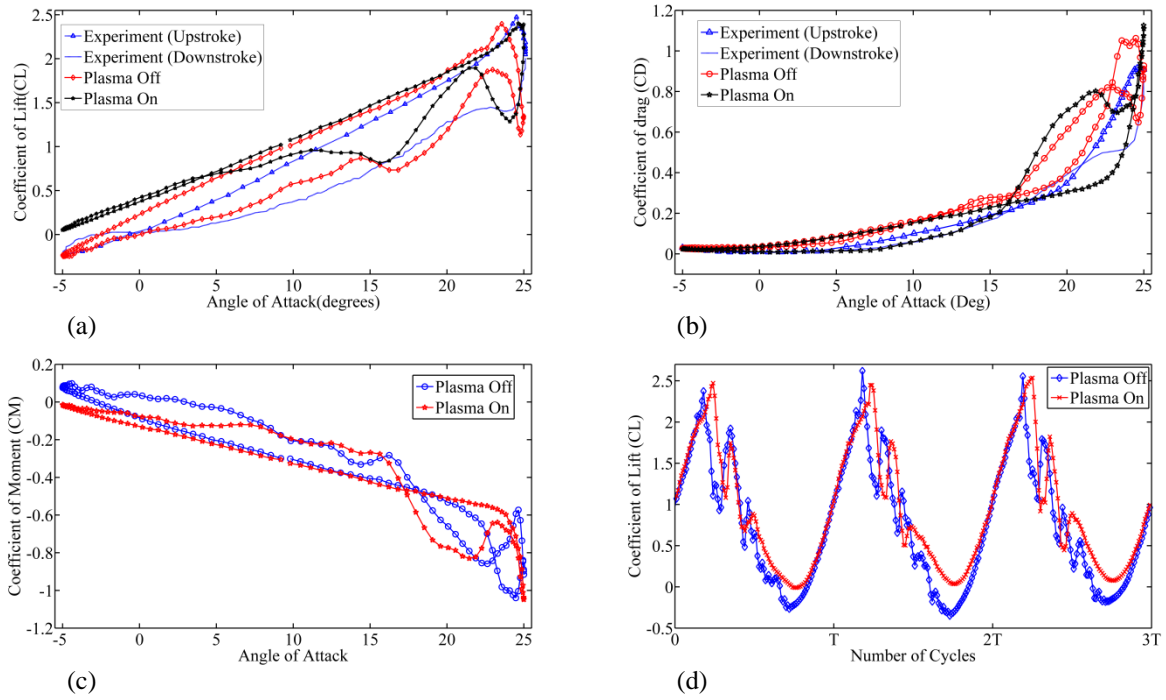
FIG. 6. Comparison of airfoil characteristics for co-flow actuation at the leading edge (a) Coefficient of Lift (C_L) against angle of attack (b) Drag (C_D) against angle of attack (c) Moment (C_M) against angle of attack (d) Time dependent plots showing lift (C_L) during the last 3 cycles of each simulation with and without plasma actuation
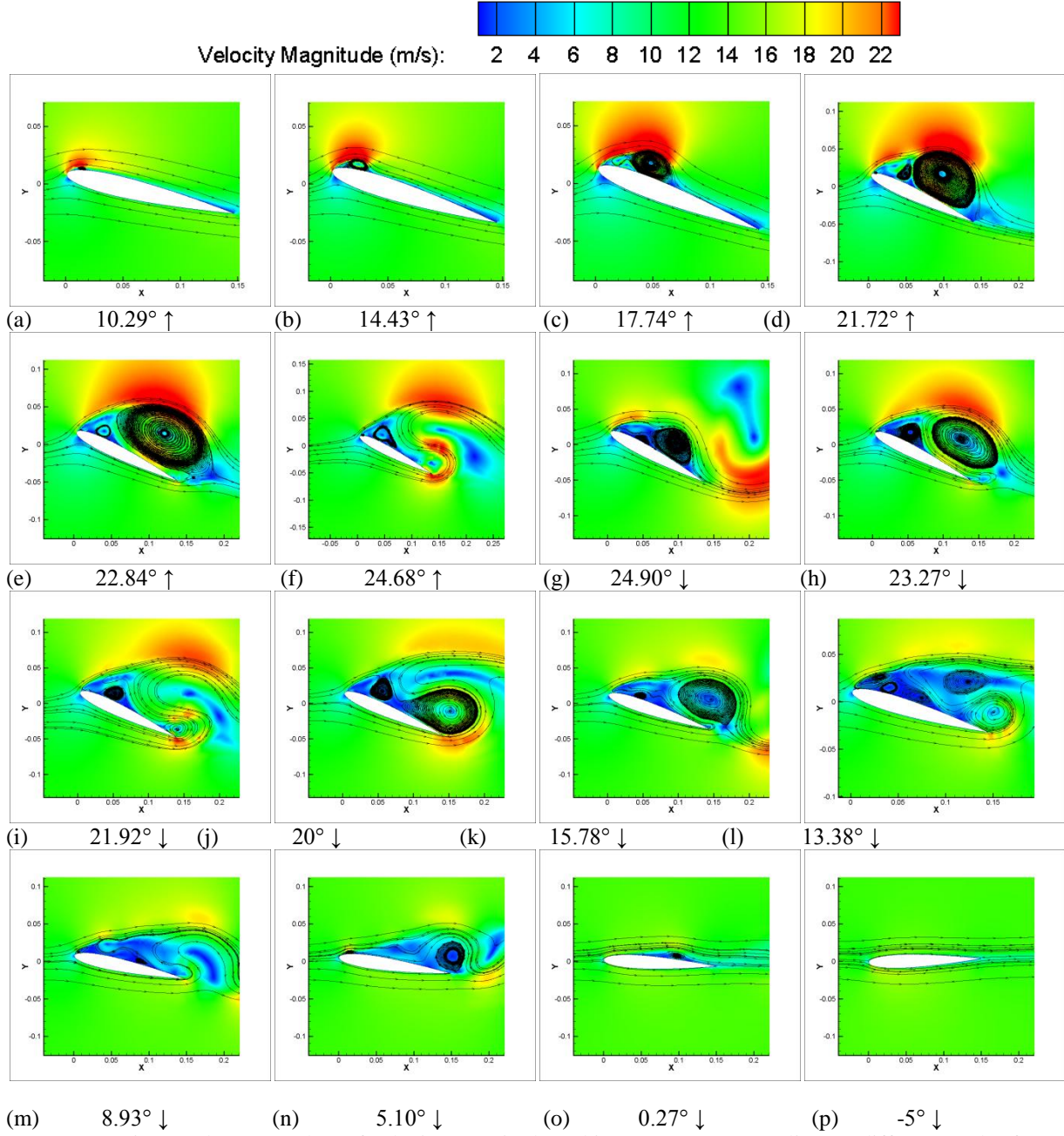
FIG. 7. Superimposed contour plots of velocity magnitude and instantaneous streamlines at different angles for a simulation with steady plasma actuation in co-flow arrangement at the leading edge (a) Start of Cycle (b) Attached flow with no signs of flow reversal (c) Flow is still attached (d) Onset of flow reversal and a tiny bubble formed at the Leading Edge (e) Formation of the LEV (f) The LEV grows is size (g) Maximum strength of LEV (h) Stalled Airfoil after the LEV has been shed (i) A secondary vortex is formed as the airfoil pitches down (j) the Secondary Vortex lifts off the surface (k) Flow beginning to reattach at the Leading edge while there are residual eddies and disturbances convecting towards the trailing edge (l) Reattached flow at the Leading Edge (m) Almost attached flow except at the trailing edge (n) attached flow (o) Smoothly attached flow as the airfoil is at a near zero angle of attack (p) Lowest angle of attack
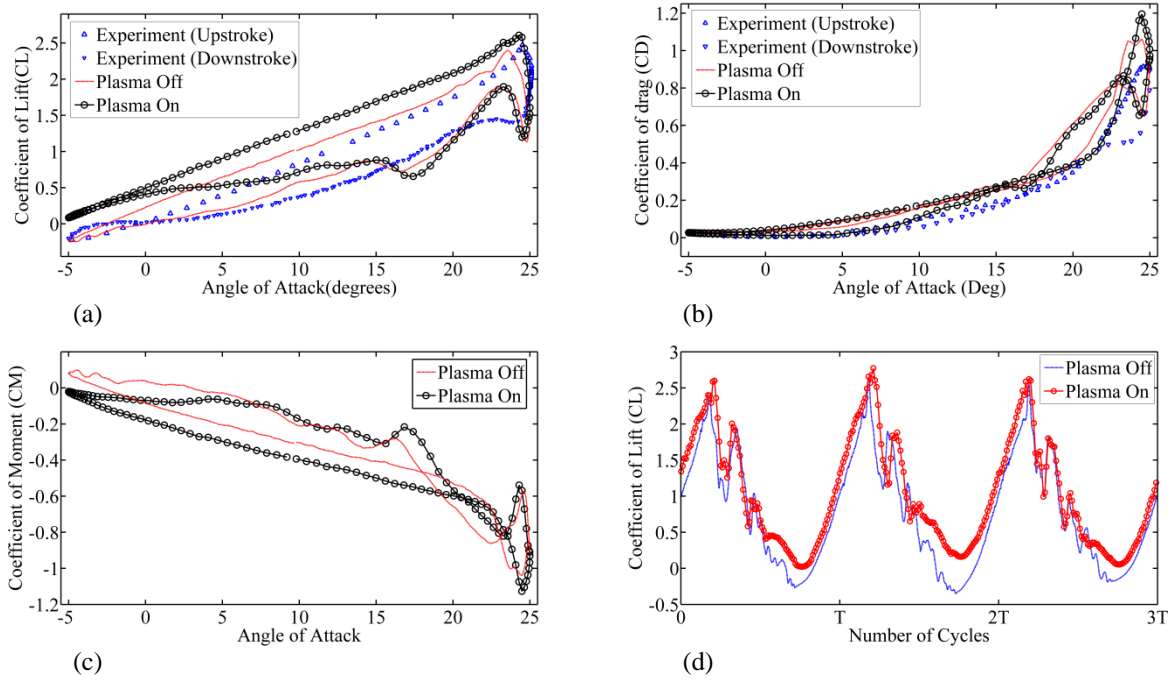
18

FIG. 8. Comparison of airfoil characteristics for counter-flow actuation at the leading edge (a) Coefficient of Lift (C_L) against angle of attack (b) Drag (C_D) against angle of attack (c) Moment (C_M) against angle of attack (d) Time dependent plots showing lift (C_L) during the last 3 cycles of each simulation with and without plasma actuation
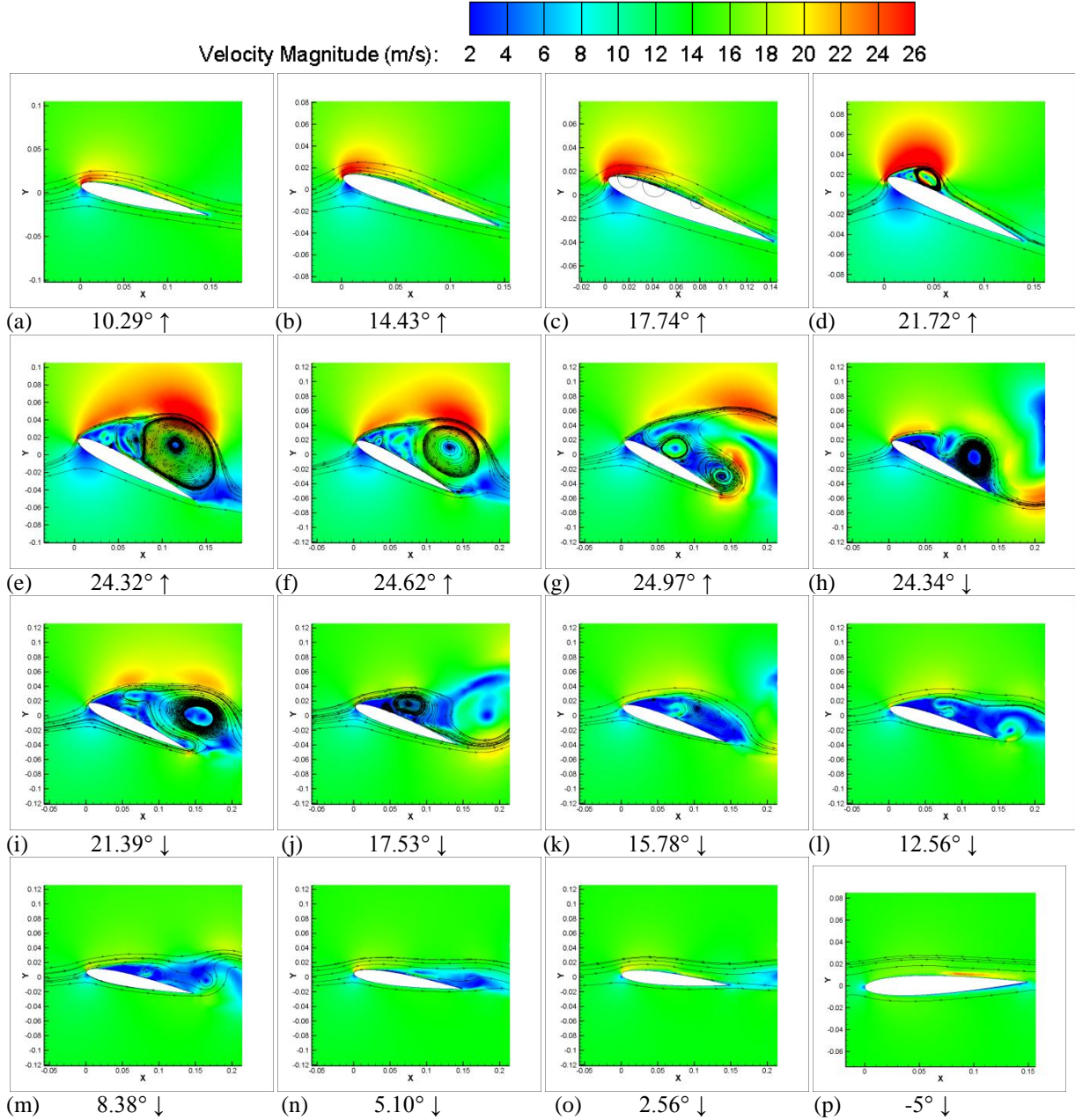
FIG. 9. Superimposed contour plots of velocity magnitude and instantaneous streamlines at different angles for a simulation with steady plasma actuation in counter-flow arrangement at the leading edge (a) Just after the start of the cycle a tiny eddy can be seen (b) A premature LEV (c) The LEV grows is size and is convected downstream (d) LEV at its maximum strength (e) The LEV has lifted off the surface (f) Stalled airfoil (g) Formation of the secondary vortex (h) The secondary vortex is shed at the trailing edge (i) Stall (j) Large recirculation regions above the suction surface (k) A recirculation bubble is shed which lowers the lift again (l) Turbulent flow separated region beyond the leading edge (m) Flow remains separated and turbulent (n) Presence of eddies even at a low angle of attack (o) Tiny disturbances created by the actuator even at zero angle of attack (p) lowest angle of attack
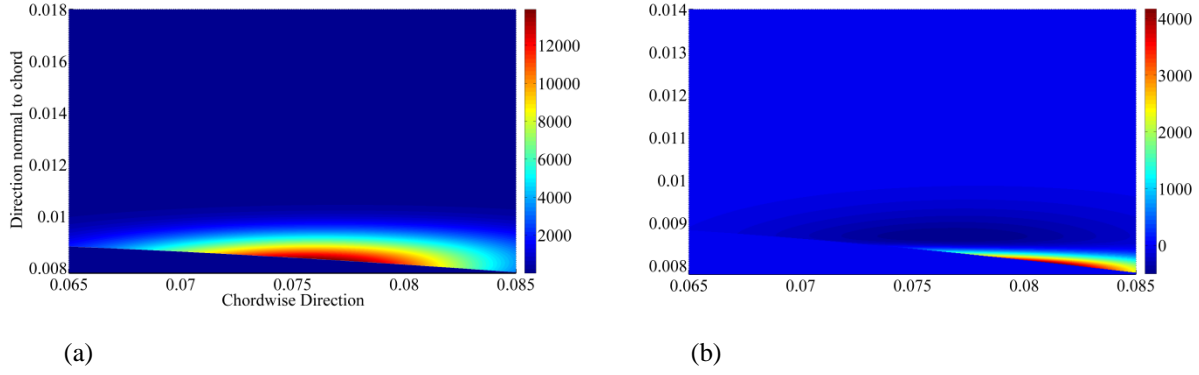
FIG. 10. Contour plots showing the location, distribution and magnitude of the force due to the plasma actuator at the mid chord region (a) Horizontal Force (b) Vertical force

FIG. 11. Comparison of airfoil characteristics for co-flow actuation at the mid chord location (a) Coefficient of Lift (C_L) against angle of attack (b) Drag (C_D) against angle of attack (c) Moment (C_M) against angle of attack (d) Time dependent plots showing lift (C_L) during the last 3 cycles of each simulation with and without plasma actuation

FIG. 12. Superimposed contour plots of velocity magnitude and instantaneous streamlines at different angles for a simulation with steady plasma actuation in co-flow arrangement at the mid chord. (a) Beginning of the cycle, (b) attached flow, (c) onset flow separation at the leading edge as tiny bubbles are formed, (d) formation of the LEV, (e) the LEV grows in size and is convected downstream, (f) the LEV is shed at the trailing edge, (g) stalled airfoil, (h) formation of the secondary vortex as the airfoil pitches down which causes a jump in lift, (i) the secondary vortex lifts off the surface, (j) disturbances in the flow at the leading edge seem to be getting mitigated at the mid chord region due to the plasma actuator, (k) the effect of the actuator can be clearly seen as it injects momentum into the flow separation region causing the flow to reattach, (l) separated flow but reduction of the size of the separated flow region, (m) better attachment of the flow and reduction of turbulence at the trailing edge due to the presence of the actuator, (n) attached flow at the leading edge, (o) reattached flow over the entire airfoil, (p) lowest point in the cycle and the infusion of momentum due to the plasma actuator can be observed from the local inflation in velocity magnitude near the mid chord location.
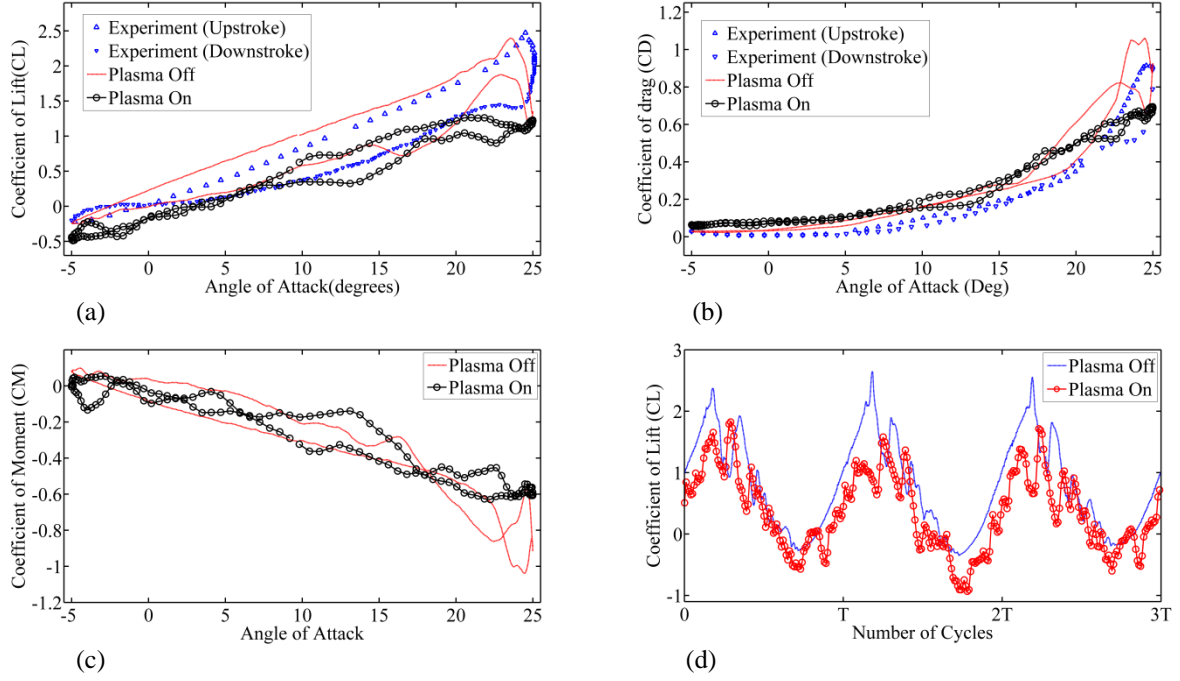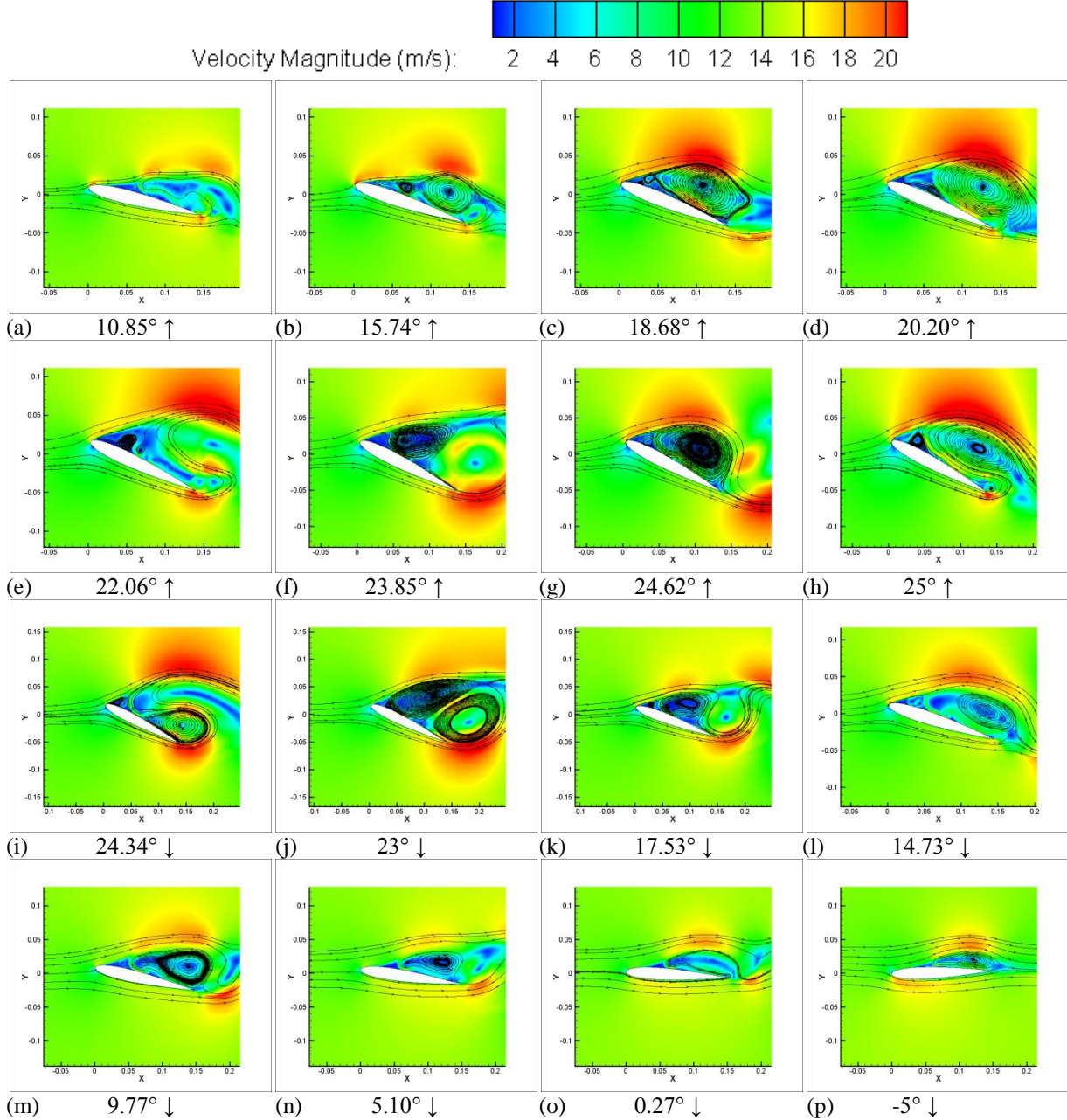
FIG. 13. Comparison of airfoil characteristics for counter-flow actuation at the mid chord location (a) Coefficient of Lift (C_L) against angle of attack (b) Drag (C_D) against angle of attack (c) Moment (C_M) against angle of attack (d) Time dependent plots showing lift (C_L) during the last 3 cycles of each simulation with and without plasma actuation

FIG. 14. Superimposed contour plots of velocity magnitude and instantaneous streamlines at different angles for a simulation with steady plasma actuation in counter-flow arrangement at the mid chord (a) Separated flow after the leading edge just after the start of the cycle (b) The counter flow actuator at the mid chord generates a anticlockwise rotating large vortex which suppresses the growth of the clockwise rotating laminar separation bubble (c) The separation region grows larger (d) The vortex lifts off the surface (e) The LEV is suppressed by the influence of the actuator (f) The growth of the LEV is limited beyond the mid chord (g) The separation regions coalesce to form a big vortical structure enveloping the entire suction surface (h) The vortex sheds off the trailing edge leading (i) The reversed flow from creates another vortex at the trailing edge as the airfoil pitches down (j) Another secondary vortex is formed at the leading edge while the trailing edge vortex is already present (k) The actuator increases the size of the separation region (l) Flow sucked off the trailing edge forms another vortex over the trailing edge (m) Flow past the leading encountering the adverse pressure gradient at the mid chord is forced into a recirculation region (n) Flow continues to be separated (o) Even at a zero angle of attack, the adverse pressure bump at the mid chord created by the actuator creates a recirculation bubble at that location (p) Lowest angle of attack

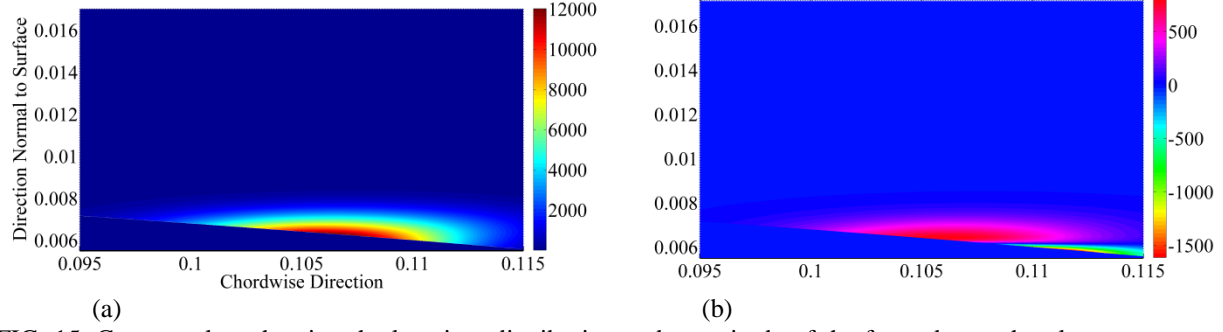(a)   (b)

FIG. 15. Contour plots showing the location, distribution and magnitude of the force due to the plasma actuator at the trailing edge (a) Horizontal Force (b) Vertical force
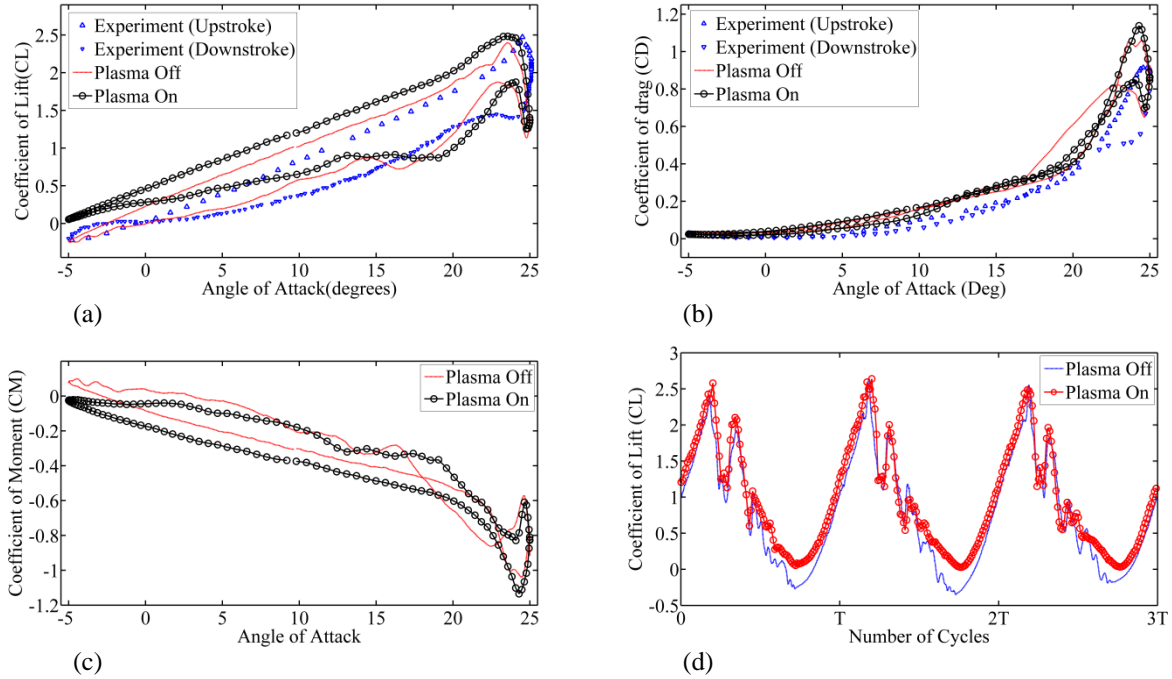

(a)   (b)

(c)   (d)

FIG. 16. Comparison of airfoil characteristics for co-flow actuation at the trailing edge (a) Coefficient of Lift (C_L) against angle of attack (b) Drag (C_D) against angle of attack (c) Moment (C_M) against angle of attack (d) Time dependent plots showing lift (C_L) during the last 3 cycles of each simulation with and without plasma actuation
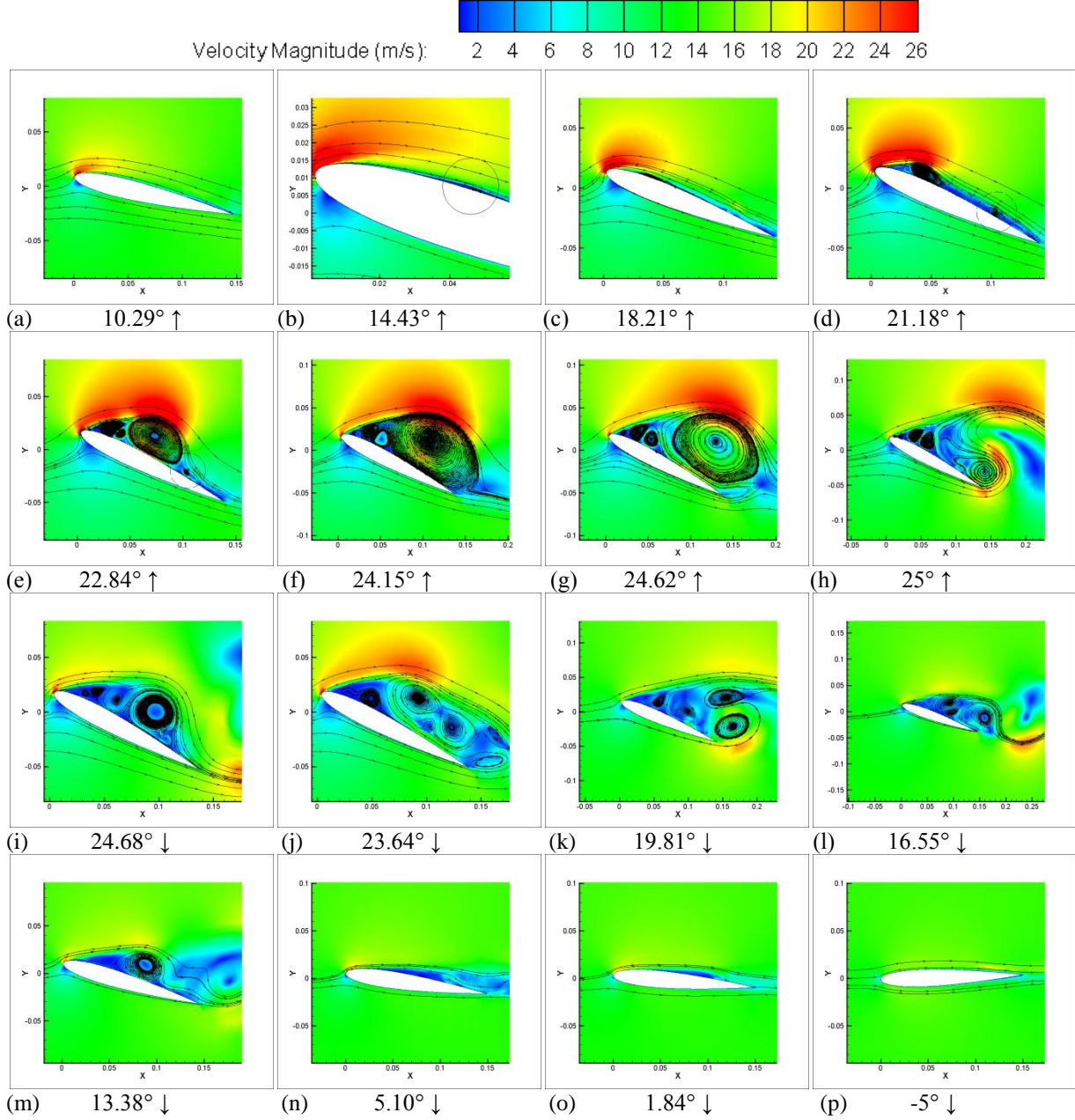
FIG. 17. Superimposed contour plots of velocity magnitude and instantaneous streamlines at different angles for a simulation with steady plasma actuation in co-flow arrangement at the trailing edge (a) Attached flow at the start of the cycle (b) Onset of flow reversal at the leading edge (c) The separation layer at the leading edge grows as the airfoil pitches up while the actuator reduces the separation layer at the trailing edge (d) The leading edge vortex is formed and the dotted circle shows the effect of the actuator as it keeps the separation layer from growing and prevents formation of small turbulent eddies (e) As the LEV grows and convects downstream and meets the actuator as shown by the dotted circle (f) The LEV has grown to its maximum size (g) The LEV lifts off the trailing edge (h) Stalled airfoil (i) The secondary vortex is formed as the airfoil pitches down (j) Infusion of momentum at the trailing edge causes the separation region to break (k) The recirculation bubbles are shed off (l) The actuator reduces the size of the wake (m) The separation region reduces and the flow starts reattaching at the trailing edge (n) The actuator reduces the separation layer at the trailing edge as the angle of attack gets lower (o) Reattached flow (p) Lowest angle of attack
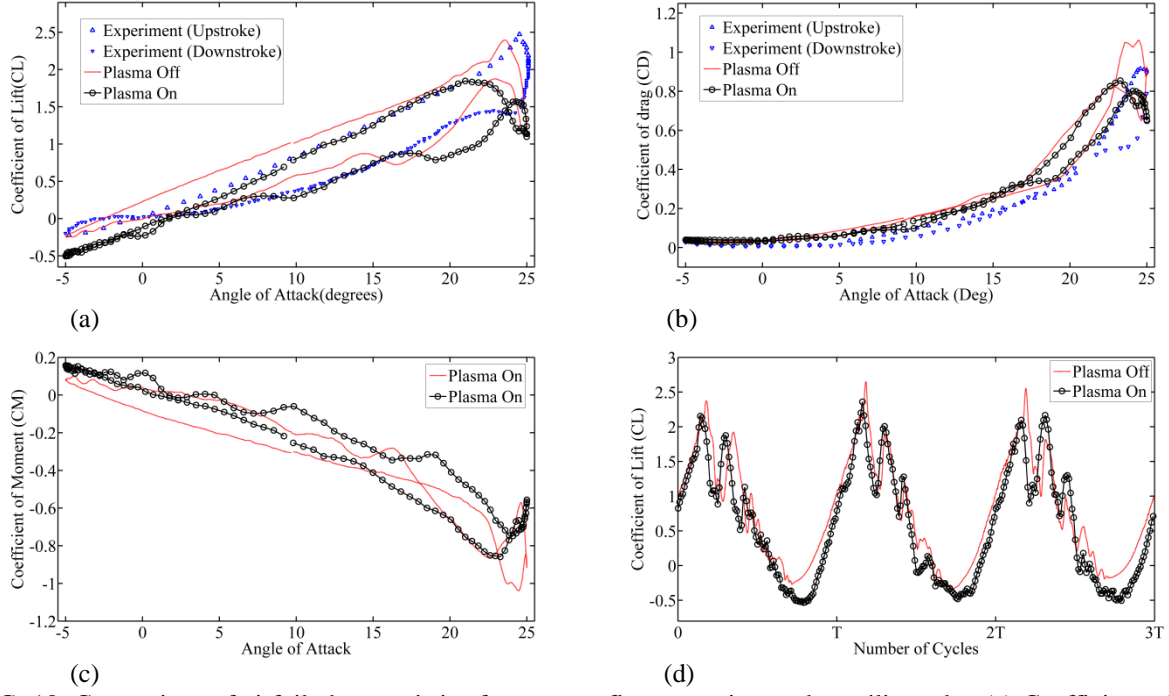
FIG. 18. Comparison of airfoil characteristics for counter-flow actuation at the trailing edge (a) Coefficient of Lift (C_L) against angle of attack (b) Drag (C_D) against angle of attack (c) Moment (C_M) against angle of attack (d) Time dependent plots showing lift (C_L) during the last 3 cycles of each simulation with and without plasma actuation
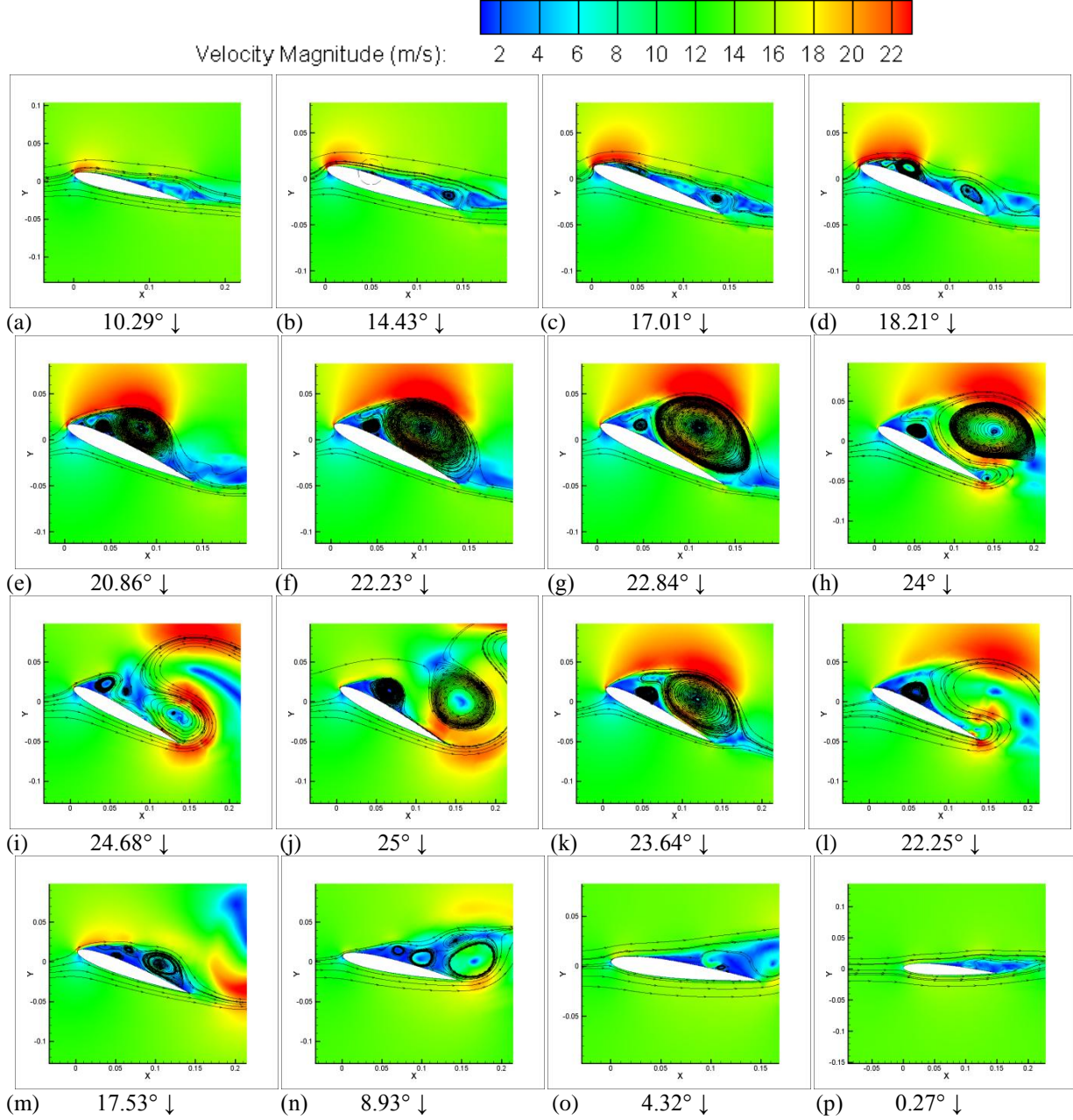
FIG. 19. Superimposed contour plots of velocity magnitude and instantaneous streamlines at different angles for a simulation with steady plasma actuation in counter-flow arrangement at the trailing edge (a) Just after start of the cycle, attached flow at the leading edge and separated flow at the trailing edge due to the counter flow arranged actuator (b) The dotted circle shows the onset of flow reversal at leading edge (c) The separation bubble at the leading edge grows alongwith with the forced disturbance at the leading edge (d) Premature formation of the LEV (e) As the LEV grows and convects downstream it is resisted by the actuator at the trailing edge (f) LEV at its maximum strength (g) LEV is shed (h) Stall (i) As the airfoil pitches down, flow reversal and suction from the trailing edge is accentuated by the actuator which results in the formation of a recirculation bubble at the trailing edge (j) At the highest angle of attack, this trailing edge vortex can be seen in the wake, while another secondary vortex has started to form at the leading edge (k) The secondary vortex is attached to the surface for a long period of time as it pitches down (l) Another period of stall as the vortex is shed (m) The presence of the actuator results in increase in the size of the separation region near the trailing edge (n) Smaller turbulent eddies (o) The effect of the actuator can be seen here as it creates a bump due to the adverse pressure gradient and incoming flow passes over it (n) Attached flow at the leading edge at zero angle of attack while flow remains separated at the trailing edge
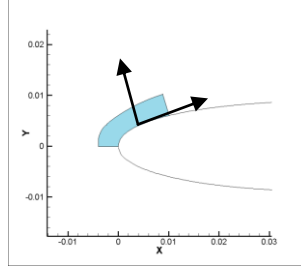
FIG. 20. Schematic Representation of the force vectors for the special case of reversing the normal component of the force to act in the outward normal direction to the airfoil surface
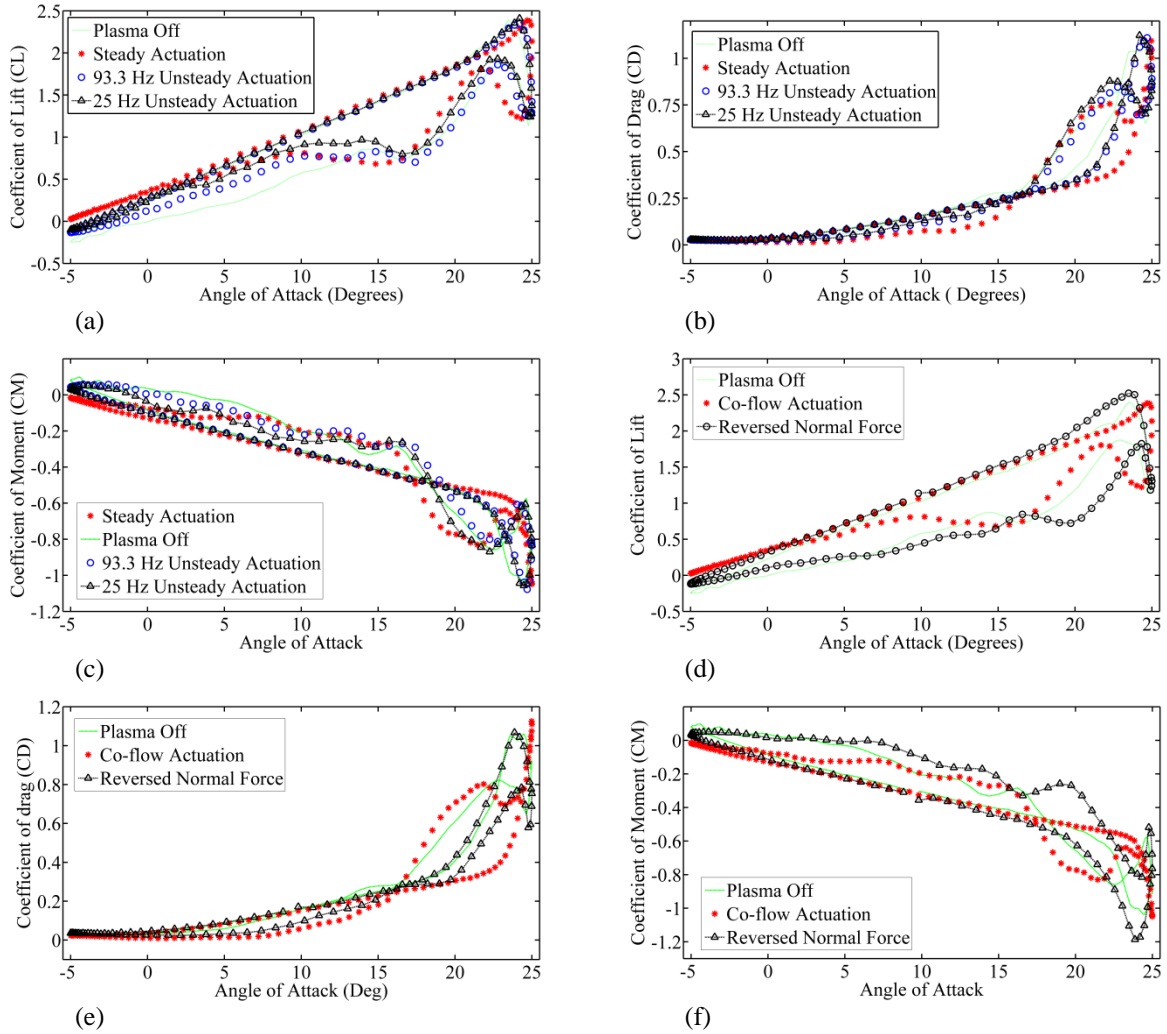

(a) (b) (c) (d) (e) (f)

FIG. 21. Characteristic curves for unsteady plasma actuation and reversal of the normal force (a) Coefficient of Lift (C_L) for unsteady actuation (b) Coefficient of Drag (C_D) for unsteady actuation (c) Coefficient of Moment (C_M) for unsteady actuation (d) Coefficient of Lift (C_L) for reversed normal force (e) Coefficient of Drag (C_D) for reversed normal force (f) Coefficient of Moment (C_M) for reversed normal force